Spin-Order Effects of Single-Atom Catalyst on Electrocatalytic Oxygen Reduction

Yi-jie Chen,[1] Jun Wen,[1] Zhi-rui Luo,[1] Fu-Li Sun,[1] Wen-xian Chen,[1] Gui-lin Zhuang*[1,2]

[1]H-PSI Computational Chemistry Lab, Institute of Industrial Catalysis, State Key Laboratory Breeding Base of Green-Chemical Synthesis Technology, College of Chemical Engineering, Zhejiang University of Technology, Hangzhou 310032, P.R. China.

* Corresponding Author, Email: glzhuang@zjut.edu.cn

[2]Key Laboratory of Functional Molecular Solids Ministry of Education, College of Chemistry and Materials Science, Anhui Normal University, Wuhu 241002, Anhui, P.R. China.

Abstract

Magnetic property (spin order) of support is of great importance in the rational design of heterogeneous catalysts. Herein, we taken the Ni-supported ferromagnetic $CrBr_3$ support ($Ni_x/CrBr_3$) to thorough investigate the effect of spin-order on electrocatalytic oxygen reduction reaction (ORR) via spin-polarized density functional theory (DFT) calculations. Specifically, Ni loading induces anti-ferromagnetic coupling in Ni-Cr, leading to a transition from ferromagnetic (FM)-to-ferrimagnetic (FIM) properties, while Ni-Ni metallic bonds create a robust ferromagnetic direct exchange, benefiting the improvement of the phase transition temperature. Interestingly, with the increase of Ni loading, the easy magnetic axis changes from out of plane (2D-Heisenberg) to in plane (2D-XY). The adsorption properties of $Ni_x/CrBr_3$, involving O_2 adsorption energy and configuration, are not governed by the *d*-band center and strongly correlate with magnetic anisotropy. It is noteworthy that the applied potential and electrolyte acidity triggers spin-order transition phenomena during the ORR and induces the catalytic pathway change from the $4e^-$ ORR to $2e^-$ ORR with the excellent onset potential of 0.93 V/RHE, comparable to the existing most excellent noble-metal catalysts. Generally, these findings offer new avenues to understand and design the heterogeneous catalysts with magnetic support.

Keywords: Magnetic Support; Spin order; *d*-band Center Theory; Heterogeneous Catalyst

1. Introduction

Hydrogen peroxide (H_2O_2), renowned for its green and environmentally friendly properties, has catalyzed extensive research efforts aimed at developing synthetic methods, largely fueled by its diverse industrial applications, including textile bleaching[1], chemical synthesis[2], papermaking[3], pharmaceuticals[4], and water purification[5]. Currently, industrial H_2O_2 production primarily depends on the costly and polluting Riedl-Pfleiderer process, involving alkyl anthraquinone oxidation and hydrogenation.[6-9] Fortunately, the direct electrosynthesis of H_2O_2 from H_2 and O_2 through the two-electron oxygen reduction reaction ($2e^-$ ORR) presents a promising alternative. This strategy offers lower energy consumption, environmental friendliness, and reduced transportation and storage risks, making it suitable for small-scale and even in situ production.[10-12] Despite larger development (e.g. noble-metal,[13-15] metal oxide,[16-18] carbon material[19, 20] and so on) regarding the rational design of electrocatalysts for $2e^-$ ORR, however, available electrocatalysts for $2e^-$ ORR suffer from limited activity and selectivity, hindering widespread commercial adoption. Thus, finding a high-performance electrocatalyst for $2e^-$ ORR is crucial as an alternative to the Riedl-Pfleiderer method.

Essentially, H_2O_2 is partially produced from O_2 through the ORR process on the cathode. O_2 activation relies on metal site back-donation; higher back-donation yields two adsorbed oxygen, while lower levels fail to activate O_2. Hence, optimizing back-donation of metal site is crucial for catalyst design to enhance H_2O_2 performance. The back-donation ability of metal site is closely related with metal-support interaction.[21-25] In this vein, the intricate behavior is typically evaluated using the *d*-band center theory pioneered by J. K. Nørskov,[26, 27] which mainly gauges the electron orbital freedom between metal and support. However, for ferromagnetic support and paramagnetic metal site, where metal site-loading may alter the spin order population of magnetic support,[28] the electronic properties associated with spin degree of freedom play a considerable role in metal-support interaction compared to *d*-band center. Surprisingly, the investigation into the effects of spin-order interactions on metal-

support interaction under the spin degree of freedom has been overlooked.

Here, we utilized DFT calculation to study the catalytic activity and selectivity of ORR on Ni-loaded $CrBr_3$ under applied potential. Specifically, three representative catalysts with different loading, $Ni_1/CrBr_3$, $Ni_2/CrBr_3$ and $Ni_8/CrBr_3$, show different magnetic properties from pristine $CrBr_3$ support. Consequently, O_2 adsorption properties (configuration, adsorption energy) on them cannot obey *d*-band center theory but relies on the magnetic anisotropy. Furthermore, the introduction of a metal bond coordinated directly to the active site weakens the adsorption of O_2 on Ni site. Interestingly, the applied potential can induce spin-order transition between two different AFM states. Additionally, a mutual transition between $4e^-$ ORR and $2e^-$ ORR selectivity on the catalyst was observed under different reaction conditions. Furthermore, three catalysts exhibit remarkable onset potentials comparable to the existing most excellent noble-metal catalysts.

2. Computational details

Spin-polarized DFT calculations are performed utilizing the Vienna ab initio simulation package (VASP 6.3.1) code.[29] Exchange-correlation interaction in Kohn-shame equation was described by Perdew-Burke-Ernzerhof (PBE) with the framework of the generalized-gradient approximation (GGA).[30, 31] Projector augmented wave (PAW) potential, featuring the computational efficiency of the ultrasoft pseudopotential and the accuracy of plane wave method, was adopted in this treatment of ion-electron interaction.[32] Because of self-interaction error of pure DFT method, which is failed to describe the strong-correlated electrons, the GGA + *U* strategy was utilized to correct the result of exchange interaction energy.[33] The *U* value of 3.65 eV for Cr and 5.64 eV for Ni were evaluated by the linear response method (see Figure S5).[34] In all calculations, the energy cutoff of 500 eV was used to expand the plane wave basis set. The Brillouin zone is sampled by the Γ-centered Monkhorst-Pack scheme[35] using a grid of 4 × 4 × 1 for structural optimization and 10 × 10 × 1 for electronic structure and magnetic properties calculations. During the all calculations, the energy and force criteria are 10^{-5} eV and 0.02 eV/Å, respectively, and the DFT-D3 method was used to

correct the weak vdW interaction.[36] For the calculation of magnetic anisotropy energy (MAE), the spin-orbit coupling (SOC) effect was considered. Concerning the periodicity effects and computational efficiency, a 2 × 2 × 1 supercell calculation was employed for $Ni_1/CrBr_3$ and $Ni_2/CrBr_3$, while a unit cell calculation was used for $Ni_8/CrBr_3$. The energy convergence criteria are improved 10^{-8} eV, respectively. To simulate the 2D structure of $Ni_x/CrBr_3$, 20 Å vacuum space is added above monolayer $Ni_x/CrBr_3$. Electronic charge is evaluated using the Bader charge analysis method and the differential charge density is visualized using VESTA.[37] The VASPKIT code was used for postprocessing of the VASP computational data.[38] The binding energy (E_b) is typically calculated as follows eq 1:[39]

$$E_b = (E_{TMn@CrBr3} - E_{CrBr3} - nE_{TM}) / n \quad (1)$$

Where $E_{TMn@CrBr3}$ and E_{CrBr3} represent the energy of $CrBr_3$ with the TM atom and the $CrBr_3$ monolayer, respectively. E_{TM} indicate the energy of the TM single atom in vacuum while n denotes the number of TM atoms.

The dependence of electronic potential on electrocatalytic property were investigated by using a uniform charge background to compensate the surface excess charges.[40] The aqueous solvent environment was described under implicit solvent models by the VASPsol code.[41, 42] The relative permittivity was set to 80 to simulate aqueous electrolytes. The effective surface tension parameter in VASPsol was 0 to neglect the cavitation energy contribution. The linearized Poisson-Boltzmann model with a Debye length of 3.0 Å simulates the compensating charge. In order to understand the reaction mechanism at various electrode potentials, the potential applied to the electrochemical interface was simulated by introducing or removing electrons (Δn) to the supercell.

The potential energy (E) of the system is defined by eq 2.

$$E = E_{DFT} - \Delta n(V_{sol} + \Phi_q / e) \quad (2)$$

where E_{DFT} is the energy calculated by DFT, V_{sol} is the electrostatic potential of the native electrolyte, and -Φq is the work function of the charged system. The relationship between Φq and the corresponding electrode potential of the reference

standard hydrogen electrode (SHE) scale is expressed in eq 3.

$$U_q(V/SHE) = -4.6V - \Phi_q / e \quad (3)$$

where 4.6 V is the work function of the H_2/H^+ couple under standard conditions.

The E-U_q point follows a quadratic function as eq 4:

$$E(U_q) = -\frac{1}{2}C(U_q - U_0)^2 + E_0 \quad (4)$$

where U_0, C, and E_0 are the fitted value of the zero-charge potential (PZC), the fitted value of the capacitance of the corresponding system, and the fitted value of the energy of the system at PZC, respectively.

The relationship between the SHE and the reversible hydrogen electrode (RHE) versus pH follows eq 5.

$$U_{RHE} = U_{SHE} + k_B T \ln(10)\, pH / e \quad (5)$$

The $4e^-$ ORR mechanism in acidic media is listed as follows, detailed ORR catalytic processes are presented in Figure S1.

$$O_2 + H^+ + e^- + * \rightarrow *OOH \quad (6)$$

$$*OOH + H^+ + e^- \rightarrow *O + H_2O \quad (7)$$

$$*O + H^+ + e^- \rightarrow *OH \quad (8)$$

$$*OH + H^+ + e^- \rightarrow * + H_2O \quad (9)$$

The adsorption energy of the reaction intermediates *OOH, *O and *OH is calculated as follows：

$$E_{ads}(*OOH) = E(*OOH) - E(slab) - 2E(H_2O) + \frac{3}{2}E(H_2) \quad (10)$$

$$E_{ads}(*O) = E(*O) - E(slab) - E(H_2O) + E(H_2) \quad (11)$$

$$E_{ads}(*OH) = E(*OH) - E(slab) - E(H_2O) + \frac{1}{2}E(H_2) \quad (12)$$

The Monte Carlo simulation with the metropolis algorithm based on the classical Heisenberg model is used to describe the thermal dynamics of magnetism in equilibrium states. At each temperature, ferromagnetic configurations are initially used, and 40000 sweeps are applied to ensure the system reaches equilibrium. All statistical

results are obtained from the subsequent 80000 sweeps. The real-space renormalization group with the majority rule is used to analyze the phase transition and locate the Curie temperature. All of the renormalization group Monte Carlo algorithms described here were implemented in open source software of MCSOLVER.[43]

3. Result and Discussion

3.1 Structure and Stability of $CrBr_3$ and $Ni_x/CrBr_3$

Firstly, the optimized structure of the $CrBr_3$ monolayer showcases its C_3 rotational symmetry as depicted in Figure S2. Each unit cell of this monolayer contains 2 Cr atoms and 6 Br atoms. In the $CrBr_3$ monolayer, every Cr atom is coordinated with 6 neighboring Br atoms, while each Br atom interacts with 2 adjacent Cr atoms. It is worth mentioning that the optimized two-dimensional lattice parameter of a = 6.38 Å, closely consistent with the reported value both theoretically and experimentally.[44] Additionally, the average Cr-Cr bond length measures 2.52 Å, and the average Cr-Br-Cr angle amounts to 94.5°, both of which closely correspond to data found in other reputable literature.[45-47] These findings serve as strong evidence affirming the accuracy and validity of our computational calculations.

Experimentally, monolayer $CrBr_3$ features a FM semiconductor state with a wide band gap of 2.87 eV.[48] To examine the impact of spin dynamics on catalytic performance, a study was conducted in which TM single atoms were introduced onto the monolayer $CrBr_3$ structure. The aim of this modification was to investigate the influence of these single atoms on the material's catalytic properties. According to the provided Figure 1a, two adsorption sites (H0 and H1) are considered for TM atoms on the 2 × 2 × 1 supercell of the $CrBr_3$ monolayer. The first site, H0, corresponds to the hollow site located at the center of the honeycombed structure formed by Cr atoms. The second site, H1, represents the hollow site directly above H0. The binding energy (see Figure 1b) shows that 3*d*-TM elements exhibit stable adsorption on either the H0 or H1 vacancy, indicating favorable thermodynamic stability. To obtain an optimal ORR catalyst, oxygen adsorption properties indicate that TMs adsorbed at the H0 site have poor ability to oxygen activation, while that on the H1 site has a superior capacity for

oxygen activation. Of the first transition-metal elements, Fe, Co, and Ni exhibit the most stable adsorption configuration at the H1 site and display oxygen adsorption energies of -1.63 eV, -1.54 eV, and -0.65 eV, respectively. Based on the Sabatier principle,[49, 50] we selected Ni related catalysts were selected to further explore the relationship between magnetic properties and catalytic activity.

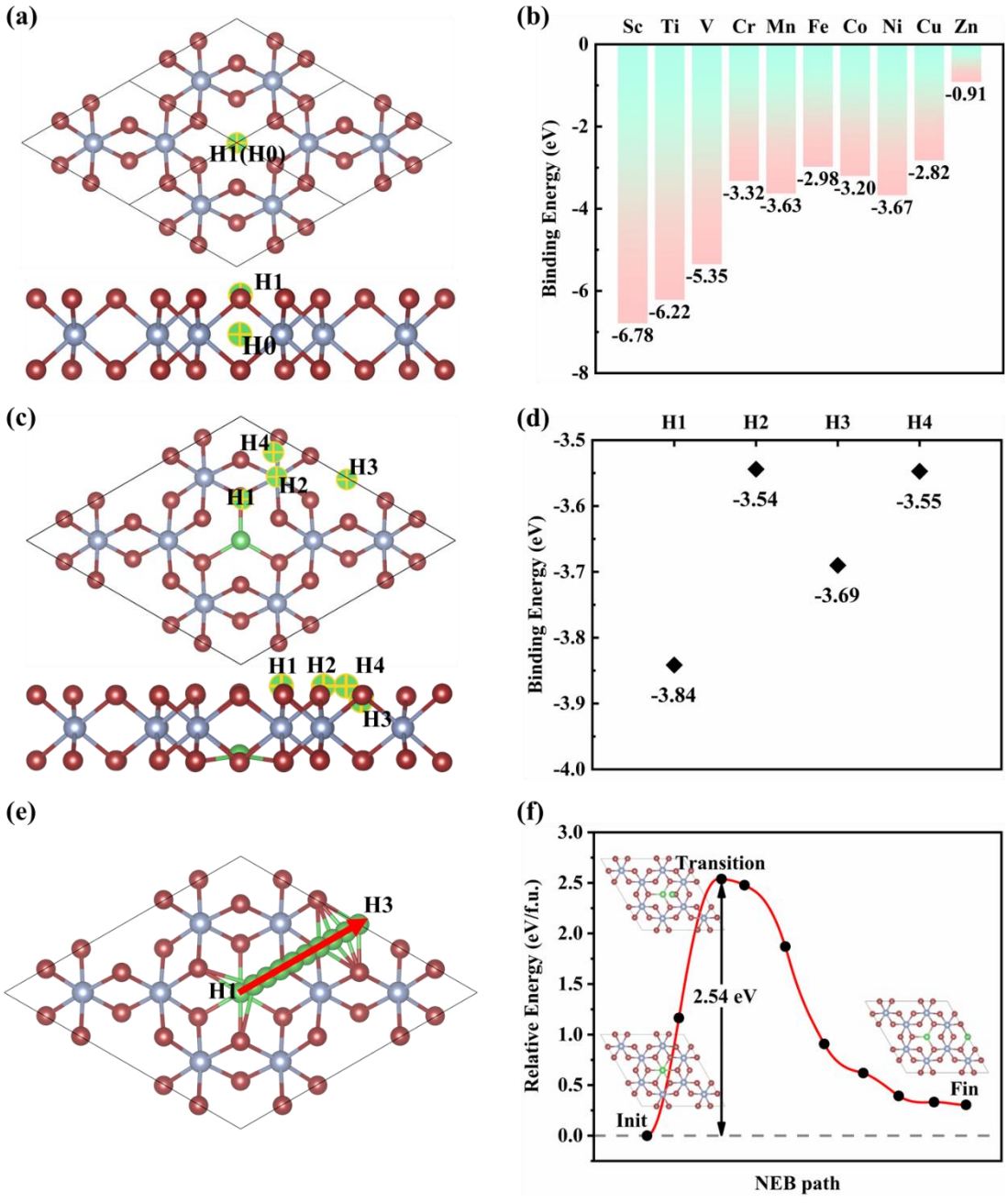

Fig. 1. The top and side views of the TM/$CrBr_3$ monolayer (a). The binding energy of TM on $CrBr_3$ monolayer (b). The top and side views of the Ni on $Ni_1/CrBr_3$ monolayer (c). The binding energy of Ni on $Ni_1/CrBr_3$ monolayer (d). The diffusion barriers of Ni

along H1 and H3 on $Ni_1/CrBr_3$ monolayer (e). The diffusion paths of Ni on the $Ni_1/CrBr_3$ monolayer (f). Cr, silver; Br, brown; Ni, green.

The supported catalysts $Ni_x/CrBr_3$ structure were formed by loading Ni onto $CrBr_3$ by varying Ni loading ratios (see Figure S3). When two Ni atoms occupies both the upper and lower surface sites of the honeycomb structure formed by Cr atoms, metal bond (d(Ni-Ni) = 2.45 Å) of Ni-Ni, compatible with the observed metal bond of Ni-Ni, is achieved. On the top sites bound to Ni-Ni metal bond, the O_2 adsorption energy will be significantly reduced from -0.65 eV to -0.31 eV. This substantial change in adsorption energy is likely to result in the selective transformation of the ORR reaction from a $4e^-$ to a $2e^-$ reaction pathway. Subsequently, the adsorption energy of O_2 for each catalyst structure was calculated and presented in Figure S4. Concerning the formation of Ni-Ni bond, three representatives, $Ni_1/CrBr_3$ without Ni-Ni bond, $Ni_2/CrBr_3$ with Ni-Ni bond and the whole occupied $Ni_8/CrBr_3$, were selected for subsequent investigations. Furthermore, it is crucial to determine the kinetic stability of Ni loading on the monolayer $Ni_1/CrBr_3$. To assess the mobility of Ni on the $Ni_1/CrBr_3$ monolayer, the diffusion barrier is calculated by using CI-NEB method.[51, 52] Furthermore, the most stable site for Ni on the $Ni_1/CrBr_3$ monolayer needs to be identified. There are four possible sites (H1, H2, H2 and H4) for Ni on the $Ni_1/CrBr_3$ monolayer, as shown in Figure 1c. It is found that that the H1 site relaxed to the $Ni_2/CrBr_3$ configuration with the lowest energy after optimization, while the H2 site was unstable. Moreover, the H3 site exhibited lower energy compared to H2 and H4 sites, as presented in Figure 1d. Consequently, the diffusion path between the H1 and H3 sites was determined, as depicted in the Figure 1e-1f. The calculated diffusion barrier is approximately 2.54 eV, confirming the kinetic stability of Ni on the monolayer $Ni_1/CrBr_3$.

3.2 The Effect of Ni-Loading on Magnetic Properties $CrBr_3$ Support

By constraining the magnetic moment of different magnetic atoms, all the possible magnetic orders of the three catalysts are summarized in the Figure 2a-b and Figure S6. After the incorporation of Ni atoms, the most stable ground states of $Ni_x/CrBr_3$ are ferrimagnetic (FIM) ground states (see Table S1), where the energy of all AFM states

are higher than that of the FIM state, indicating that $Ni_x/CrBr_3$ (x = 1, 2, 8) tends to be ferrimagnetic coupling.

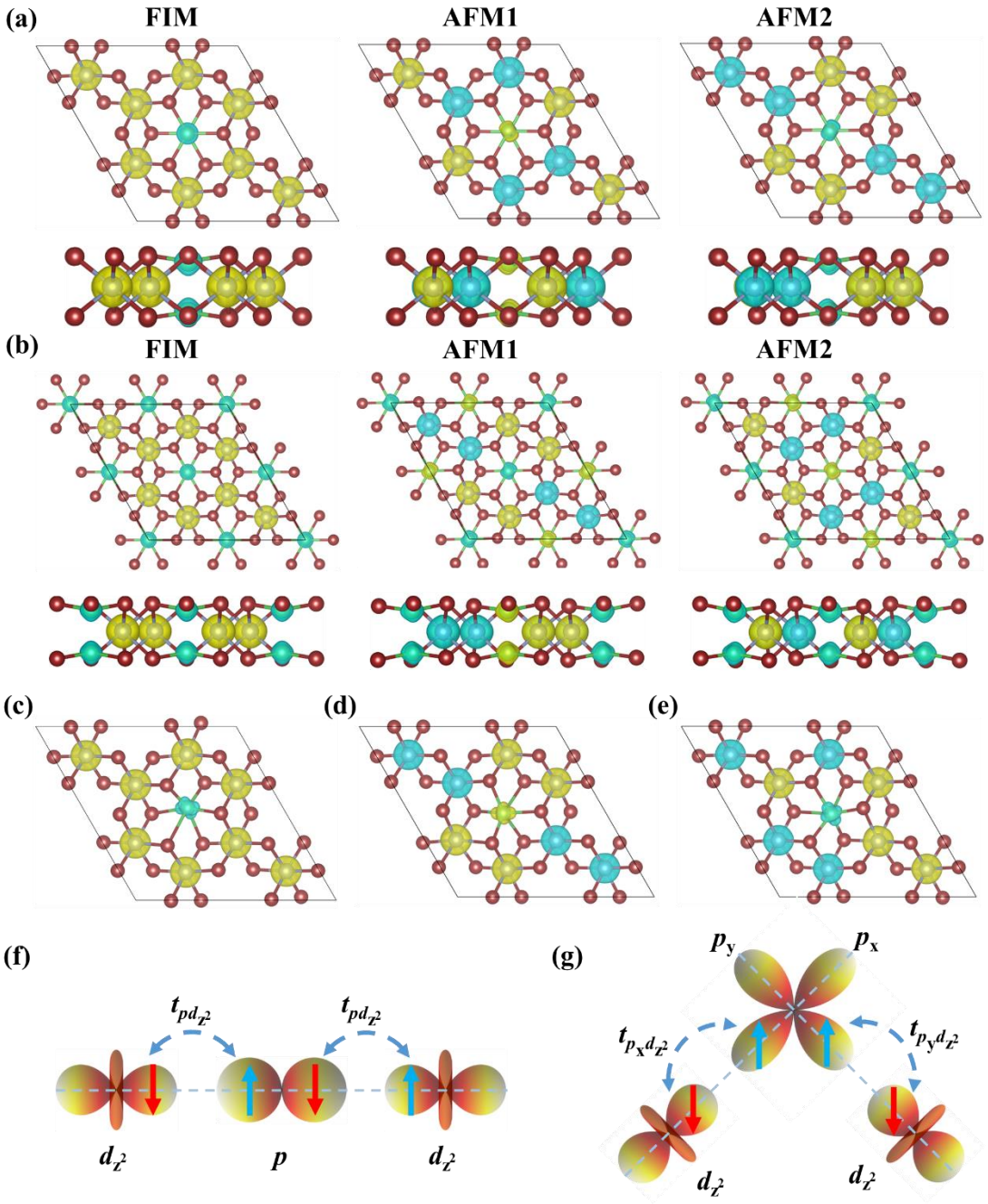

Fig. 2. Possible magnetic ordering of (a) $Ni_2/CrBr_3$, (b) $Ni_8/CrBr_3$ obtained by screening. The spin density isosurface with a value of 0.03 e/Å^3 for: (c) the FIM, (d) AFM1 and (e) AFM2 configurations of $Ni_1/CrBr_3$. The cells outlined by solid black lines are used for the calculations of magnetic structures. Goodenough-Kanamori-Anderson rules schematic. (f-g) schematic illustration of the sign in the case that bond angles are 180°

and 90°. The 180° superexchange prefer antiferromagnetic coupling, and the 90° superexchange prefer ferromagnetic coupling.

Curie temperature (Tc) is a crucial parameter for the practical application of spintronic devices. Therefore, Metropolis Monte Carlo algorithm based on the Heisenberg model was utilized to evaluate the Tc of monolayer $Ni_1/CrBr_3$, $Ni_2/CrBr_3$, and $Ni_8/CrBr_3$ following the spin Hamiltonian as follows:[53, 54]

$$H = -\sum_{i,j} J_1 S_i S_j - \sum_{k,l} J_2 S_k S_l - \sum_{m,n} J_3 S_m S_n \quad (13)$$

Where J_1, J_2 and J_3 are all defined as nearest neighbor exchange parameters, representing Cr-Cr coupling, Cr-Ni coupling and Ni-Ni coupling respectively, and S is the spin operator. By integrating the spin density of the corresponding magnetic state of $Ni_1/CrBr_3$, as shown in Figure 2(c-e) and substituting the energy obtained from the DFT calculation into eq 13, the following result was obtained:

$$E_{\mathrm{FIM}} = E_0 - 12J_{Cr-Cr}S_{Cr}S_{Cr} + 6J_{Cr-Ni}S_{Cr}S_{Ni} \quad (14)$$

$$E_{\mathrm{AFM1}} = E_0 + 4J_{Cr-Cr}S_{Cr}S_{Cr} - 2J_{Cr-Ni}S_{Cr}S_{Ni} \quad (15)$$

$$E_{\mathrm{AFM2}} = E_0 + 4J_{Cr-Cr}S_{Cr}S_{Cr} \quad (16)$$

Where E_{FIM}, E_{AFM1} and E_{AFM2} are the total energy of FIM, AFM1 and AFM2 configurations from DFT calculations. E_0 is the total energy of systems without magnetic coupling. S is the projected magnetic moment of each magnetic atom. The magnetic coupling Hamiltonian and spin density for $Ni_2/CrBr_3$ are presented in the Figure S7. In addition, the J values of $Ni_8/CrBr_3$ are calculated by using the four-states method,[55, 56] and the detailed calculation procedure can be found in the Figure S8. The calculated J values for $Ni_1/CrBr_3$, $Ni_2/CrBr_3$, and $Ni_8/CrBr_3$ are listed in the Table 1.

Table 1. The value *J* of the magnetic coupling constant of $Ni_1/CrBr_3$, $Ni_2/CrBr_3$ and $Ni_8/CrBr_3$.

	J_1/K	J_2/K	J_3/K
$CrBr_3$	27.50	0	0
$Ni_1/CrBr_3$	8.11	-8.34	0
$Ni_2/CrBr_3$	3.36	-21.32	204.77
$Ni_8/CrBr_3$	1.78	-19.52	8.58

For $Ni_1/CrBr_3$, $Ni_2/CrBr_3$ and $Ni_8/CrBr_3$ the magnetic interactions between the nearest neighboring Cr-Cr atoms with $J_1>0$ exhibit ferromagnetic coupling, while the magnetic interactions between the nearest neighboring Cr-Ni atoms with $J_2<0$ exhibit antiferromagnetic coupling. This is consistent with the analysis based on superexchange interactions. The Cr-Br-Cr bond angles are close to 90°, while the Cr-Br-Ni bond angles are close to 100° (see the Table S2). According to the Goodenough-Kanamori-Anderson (GKA) rules,[57-59] when the bond angle between cation-anion-cation approaches 90°, the superexchange interactions mediated by the anions should always result in FM coupling (see Figure 2f-g). The interactions between the nearest neighboring Ni-Ni atoms arise from direct metallic interactions within the layers.

Magnetic anisotropy plays a critical role in achieving long-range magnetic ordering in two-dimensional materials.[53, 60, 61] Herein, concerning the spin-orbit coupling interaction, the MAE of monolayer $Ni_x/CrBr_3$ ($Ni_1/CrBr_3$, $Ni_2/CrBr_3$, and $Ni_8/CrBr_3$) are calculated using the equation MAE = E_q - E_z, where E_q and E_z represent the total energy of the system along the magnetic moments in the directions q and [001], respectively. Table 2 presents the total MAE of monolayer $Ni_x/CrBr_3$ and the MAE values for individual atoms. The MAE values for monolayer $Ni_1/CrBr_3$, $Ni_2/CrBr_3$, and $Ni_8/CrBr_3$ are determined as 1420, 1150, and -305 meV/f.u. (formular unit), respectively. Due to periodicity effects in the calculations, $Ni_1/CrBr_3$ and $Ni_2/CrBr_3$ were computed using a 2 × 2 × 1 supercell, while $Ni_8/CrBr_3$ employed unit cell calculation. Consequently, the total MAE values are not comparable, but the MAE for each atom remains unchanged. In Figure 3a, the depicted MAE is derived from an extensive scan

across azimuth and polar angles, and the corresponding MAE 3D distribution scanning results are shown in Figure S9. This aligns with the findings detailed in Table 2. Notably, the MAE results reveal that $Ni_1/CrBr_3$ and $Ni_2/CrBr_3$ display perpendicular magnetic anisotropy (PMA), whereas $Ni_8/CrBr_3$ shows a deviation in the easy axis direction, residing within the xy plane. To delve deeper into the origins of the unique magnetic anisotropy observed in $Ni_x/CrBr_3$, Figure 3b presents the orbital-resolved MAE of the system.[61] In the $Ni_x/CrBr_3$, the MAE predominantly stems from the Ni-d, Cr-d, and Br-p orbitals, with the contributions of Br-d, Ni-p, and Cr-p orbitals being comparatively minor. Furthermore, with an increase in Ni content, there is a notable escalation in the contribution of the Ni-d orbital to the MAE. Simultaneously, the contribution of the Br-p orbital experiences a decline, whereas the contribution of the Cr-d orbital largely remains unchanged. Consequently, the overall MAE of $Ni_x/CrBr_3$ emerges as a result of the interplay between the Ni-d and Br-p orbitals. As illustrated in the Figure 3b, the MAE of $Ni_1/CrBr_3$ is predominantly driven by the Br-p orbital, which yields a significant positive contribution to the MAE. In contrast, for $Ni_2/CrBr_3$, the MAE is jointly determined by the Ni-d, Br-p, and Cr-d orbitals, all of which provide positive contributions to the MAE. This induces PMA of monolayer $Ni_1/CrBr_3$ and $Ni_2/CrBr_3$. For $Ni_8/CrBr_3$, the MAE is mainly influenced by the Br-p orbitals, and their contribution is negative. Despite a rise in Ni content to 100%, where Br-p orbitals contribute negatively and Ni-d orbitals play a more significant role, the overall MAE is still primarily governed by the Br-p orbitals. Consequently, the magnetic easy axis of $Ni_8/CrBr_3$ remains in the xy plane. Utilizing the spin Hamiltonian and considering the contribution of magnetic anisotropy from each atom, the temperature-dependent relationship between the average magnetic moment and magnetic susceptibility of $Ni_x/CrBr_3$ was calculated and plotted (refer to Figure 3c-f). The estimated Tc values for $Ni_1/CrBr_3$, $Ni_2/CrBr_3$, and $Ni_8/CrBr_3$ are approximately 90 K, 73 K, and 190 K, respectively. In addition, employing the same method, the Tc value for monolayer $CrBr_3$ was calculated to be approximately 42 K, consistent with the experimental result of 34 K.[44] This demonstrates the reliability of our simulation results. Generally, the $Ni_x/CrBr_3$

attain the antiferromagnetic state at room temperature. The DOS distribution diagram in Figure 3(c-f) illustrates that as the loading amount of Ni increases, $CrBr_3$ shifts from being a magnetic semiconductor to a magnetic semimetal. This transition is linked to heightened metallic properties due to the increased Ni loading, expanding the catalyst's application potential and advancing magneto-electrochemical catalysis development.

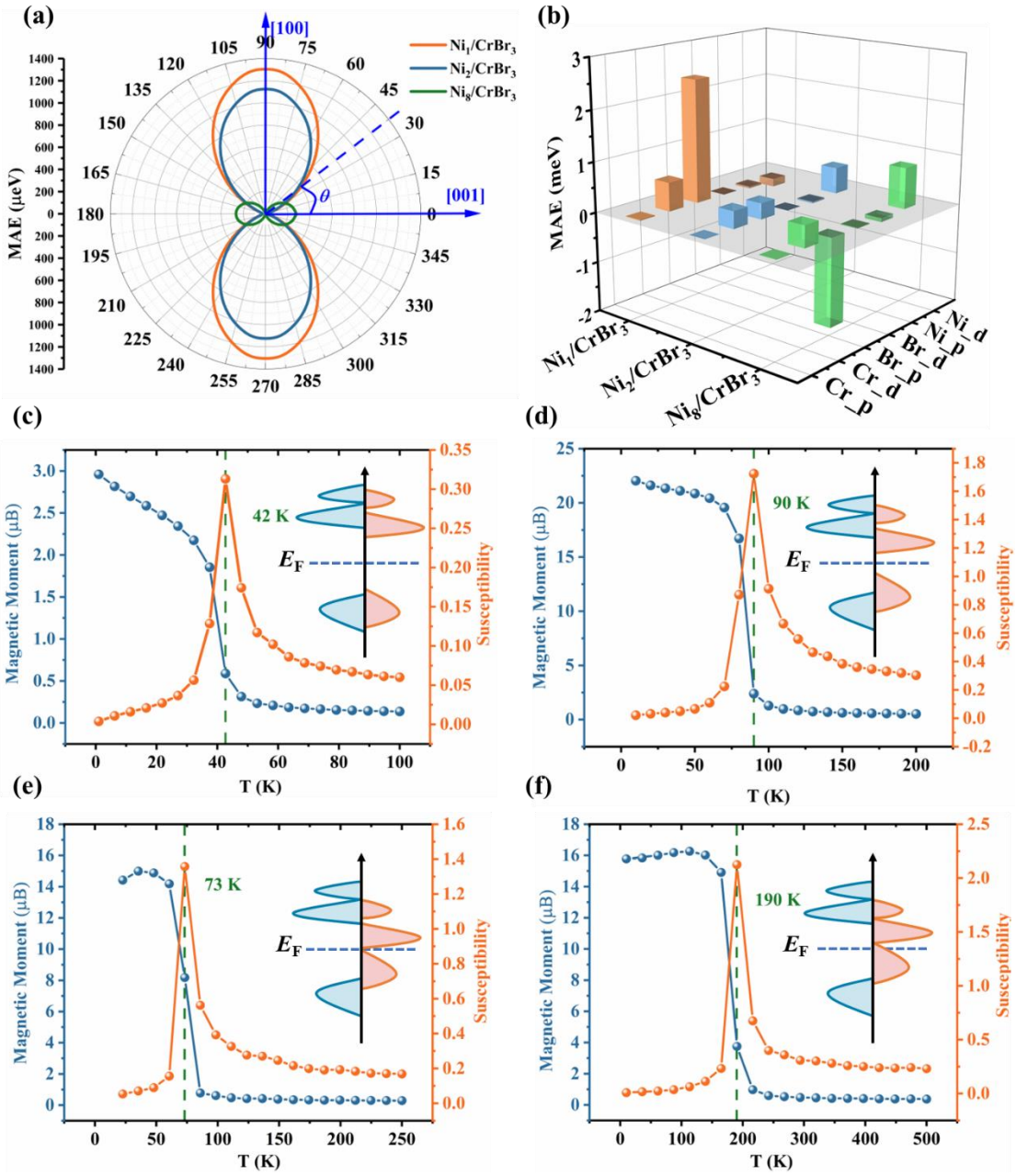

Fig. 3. (a) Dependence of the MAE on the polar angle θ for the $Ni_1/CrBr_3$, $Ni_2/CrBr_3$ and $Ni_8/CrBr_3$. (b) The contributions of Cr-p orbitals, Cr-d orbitals, Br-p orbitals, Br-d orbitals, Ni-p orbitals and Ni-d orbitals to MAE for monolayer $Ni_x/CrBr_3$. The average magnetic moment and magnetic susceptibility varying with the increasing of

temperatures for monolayer (c) $CrBr_3$, (d) $Ni_1/CrBr_3$, (e) $Ni_2/CrBr_3$, (f) $Ni_8/CrBr_3$.

Table 2. The MAE for the [100] and [010] direction, MAE of different atoms, and easy axis for monolayer $Ni_x/CrBr_3$.

System	$E_{[100]}$ - $E_{[001]}$ (μeV)	$E_{[010]}$ - $E_{[001]}$ (μeV)	MAE/Cr (μeV)	MAE/Br (μeV)	MAE/Ni (μeV)	Easy axis
$Ni_1/CrBr_3$	1420	1420	36.9	51.1	-100.5	[001]
$Ni_2/CrBr_3$	1150	1150	43.2	13.0	246.7	[001]
$Ni_8/CrBr_3$	-305	-313	113.0	-153.3	194.4	xy plane

3.3 Crucial effect of MAE on O_2 Adsorption

Essentially, the adsorption and activation of O_2 is a prerequisite of the whole ORR. Usually, oxygen adsorption on a catalyst surface generally occurs in three configurations (see Figure S1) : end-on Pauling-type (one oxygen atom coordinated to single site), side-on Griffiths-type (two oxygen atoms bonded to single site), and Yeager-type (two oxygen atoms bonded separately to two sites).[62] Figures 4(a-c) depict the most stable adsorption configurations and associated charge transfer scenarios for three $Ni_x/CrBr_3$ catalysts. In all cases, O_2 maintains a stable adsorption configuration with the O-O bond intact. Charge difference and bader charge analysis show that O_2 molecules in the adsorbed state acquire electrons from the catalyst, indicating different degrees of activation of the adsorbed O_2 molecules. Notably, the most stable O_2 adsorption configuration is the Griffiths type (side-on) for $Ni_1/CrBr_3$ (d(O-O) = 1.35 Å) and $Ni_8/CrBr_3$ (d(O-O) = 1.36 Å), while the Pauling type (end-on) for $Ni_2/CrBr_3$ (d(O-O) = 1.29 Å). Energetically, the resultant adsorption energies are -0.65 eV for $Ni_1/CrBr_3$, -0.31 eV for $Ni_2/CrBr_3$, and -0.46 eV for $Ni_8/CrBr_3$, respectively. What causes their differences?

Structurally, the adsorption site is Ni site in the $[NiBr_3]$ moiety for $Ni_1/CrBr_3$, while those are Ni site in the $[Ni_2Br_6]$ moiety for $Ni_2/CrBr_3$ and $Ni_8/CrBr_3$. Thus, the difference in adsorption energy between $Ni_1/CrBr_3$ and $Ni_2/CrBr_3$ and $Ni_8/CrBr_3$ are

attributed to the formation of Ni-Ni metal bond. Projected Density of State (PDOS) of these three catalysts (see Figure S10-11) result indicates that compared to $Ni_1/CrBr_3$, Ni-Ni metal bond for $Ni_2/CrBr_3$ and $Ni_8/CrBr_3$ enhance the *d*-band broadening and thereby reduces the d-band center, leading to weak adsorption energy. In this respect, *d*-band centers ($\varepsilon_d\uparrow$ = -0.54eV for $Ni_1/CrBr_3$, $\varepsilon_d\uparrow$ = -0.88eV for $Ni_2/CrBr_3$ and $\varepsilon_d\uparrow$ = -0.97eV for $Ni_8/CrBr_3$) also validate this conclusion. However, the adsorption-energy difference between $Ni_2/CrBr_3$ and $Ni_8/CrBr_3$ contradicts the trend of *d*-band centers. From the viewpoint of configuration, it is interesting that $Ni_2/CrBr_3$ and $Ni_8/CrBr_3$ display significantly different adsorption structures: Pauling type for $Ni_2/CrBr_3$ and Griffiths type for $Ni_8/CrBr_3$. Such tiny difference in *d*-band center leads to different adsorption configuration. Therefore, we speculate: Are there other factors than *d*-band center?

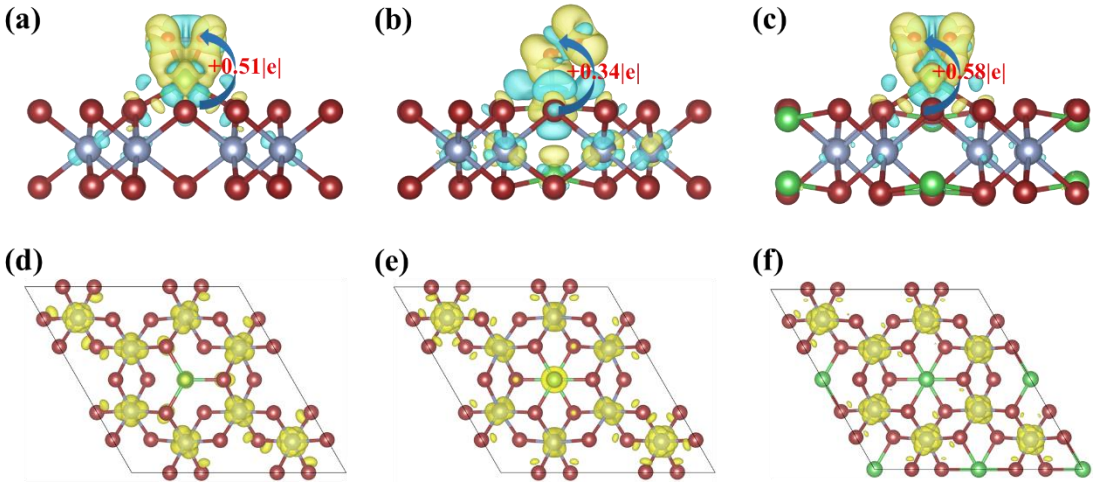

Fig. 4. (a) $Ni_1/CrBr_3$, (b) $Ni_2/CrBr_3$, (c) $Ni_8/CrBr_3$, the most stable configuration of adsorbed oxygen, and the corresponding charge transfer. (isosurface = 0.002 e/Å^3). The partial charge density corresponding to CBM of (d) $Ni_1/CrBr_3$, (e) $Ni_2/CrBr_3$, (f) $Ni_8/CrBr_3$.

The *d*-band center theory primarily focuses on the orbital degrees of freedom of electrons, often underestimating the role of spin contribution, particularly in magnetic order interactions. This is due to the relatively weaker influence of spin interactions compared to orbital interactions. However, for ferromagnetic support, the stronger magnetic interaction results in electronic structure closely tied to spin degrees of

freedom. Thus, the catalytic activity of ORR is governed by both spin-related properties as well as the *d*-band center. Aforementioned magnetic calculation result revealed both $Ni_2/CrBr_3$ and $Ni_8/CrBr_3$ feature ferrimagnetic property with Tc values of 73 K and 190 K, respectively. Moreover, $Ni_8/CrBr_3$ features spin population of 2D-XY model with easy axis of xy plane, while $Ni_8/CrBr_3$ attains the spin population of 2D-Heisenberg model to the easy axis of z-axis.

Thus, do the magnetic property (e.g. MAE) plays an important role the difference in adsorption property? Figure S12 illustrating the orientation of the easy axis when O_2 is adsorbed on the three types of catalysts. By calculating the contributions of each atomic orbital to the MAE, it was found that the contribution of O_2 to the overall MAE can be almost neglected. For $Ni_1/CrBr_3$, although the MAE orientation is along the z-axis, its *d*-band center is close to the Fermi level, resulting in strong O_2 adsorption energy. Therefore, when O_2 adsorbs on $Ni_1/CrBr_3$, d-band center plays a dominant role, leading to a preference for Griffiths-type adsorption. In contrast, for $Ni_2/CrBr_3$ and $Ni_8/CrBr_3$, which have metallic bonding, both their *d*-band centers are close to each other and farther away from the Fermi level than $Ni_1/CrBr_3$, resulting in weaker O_2 adsorption. In this case, MAE may take precedence. Specifically, when the MAE orientation undergoes an out-of-plane to in-plane transition, it causes a change in adsorption configuration from end-on to sideways adsorption. In general, orbital degrees of freedom and spin degrees of freedom jointly determine the adsorption mode of O_2 on the $Ni_x/CrBr_3$ surface. When the *d*-band center is close to the Fermi level, the adsorption energy intensity plays a leading role in the adsorption configuration of O_2. When the *d*-band center is far away from the Fermi level, the direction of MAE, that is, the easy axis, plays a dominant role in the adsorption configuration of O_2.

Furthermore, additional Partial Charge Density analysis was conducted for the $Ni_x/CrBr_3$ catalyst and presented in Figure 4(d-f), with further details provided in Figure S13. For $Ni_8/CrBr_3$, when O_2 is adsorbed on the surface of $Ni_8/CrBr_3$, the Ni atom centered at the active site of catalyzing ORR will have a strong interaction with the conduction band minimum (CBM) of the catalyst. The charge distribution on Ni atom

in the center of the CBM structure corresponding to $Ni_1/CrBr_3$ and $Ni_8/CrBr_3$ is small, indicating that Ni atom in this state has more empty orbitals at CBM, which leads to a relatively strong interaction between O_2 and Ni atom, weakens the O-O bond, and facilitates the splitting of O-O bond. This directly leads to the high selectivity of $Ni_1/CrBr_3$ and $Ni_8/CrBr_3$ catalysts for $4e^-$ ORR. For the CBM structure corresponding to $Ni_2/CrBr_3$, the central Ni atom itself carries a small amount of charge, which makes a part of the orbital filled, resulting in a weak ability to bind oxygen, and more inclined to Pauling-type, so it has better $2e^-$ ORR selectivity. Subsequently, the conclusions drawn from the catalytic reaction path will be verified.

3.4 Catalytic Performance of ORR on $Ni_x/CrBr_3$

Essentially, the electrocatalytic ORR process involves three crucial steps: (1) diffusion and adsorption of O_2 on the catalyst surface, (2) hydrogenation of the adsorbed O_2 by H^+/e^- to form products, and (3) desorption and diffusion of the final products on the catalyst surface. Regarding the hydrogenation degree of O_2 adsorption, the ORR primarily involves two electron pathways leading to either H_2O_2 or four electron pathways resulting in H_2O as products. During electrocatalytic process, both $4e^-$ ORR and $2e^-$ ORR are competing reactions, highly influenced by the adsorption configuration and activation degree of O_2.[63]

Based on the above analysis, compared to nonmagnetic catalysts, spin-order of ferromagnetic support plays an important role in the adsorption of O2. Thus, the relationship between the catalytic performance and magnetic properties on different catalysts with different converge was further explored, and the specific paths of $2e^-$ ORR and $4e^-$ ORR in different magnetic states of the above three catalysts were studied. As shown in the Figure 5, $Ni_1/CrBr_3$ mainly undergoes $4e^-$ ORR, where the potential-determining step is the last detachment step, i.e., $*OH + H^+ + e^- \rightarrow * + H_2O$. This means that the Ni-O bond on the $Ni_1/CrBr_3$ catalyst is relatively strong. In addition, the most stable adsorption configuration of O_2 on $Ni_1/CrBr_3$ is Griffiths type, in which the molecular orbitals of O_2 interact strongly with the empty *d* orbitals of Ni, weakening the O-O bond and facilitating its cleavage, which directly leads to the high selectivity

of $Ni_1/CrBr_3$ catalyst for $4e^-$ ORR. Considering the impact of the central vacant Ni-Ni pair on catalytic performance, when the catalyst is $Ni_2/CrBr_3$ or $Ni_8/CrBr_3$, both the $2e^-$ ORR catalytic activity and selectivity are significantly improved. Considering the O_2 adsorption configuration, the most stable adsorption configuration of O_2 on $Ni_2/CrBr_3$ catalyst is Pauling-type. Due to the end-on adsorption configuration, only one side of the O_2 molecule interacts with the active sites of $Ni_2/CrBr_3$, which minimizes O-O bond cleavage and inhibits the $4e^-$ ORR pathway, thus promoting the $2e^-$ ORR pathway. The O_2 adsorption configuration of $Ni_8/CrBr_3$ is Griffiths type, yet it exhibits excellent $2e^-$ ORR activity. Therefore, for $Ni_8/CrBr_3$, a simple explanation based solely on the adsorption configuration is insufficient. Through the previous discussion, spin degrees of freedom were introduced to explain the configuration of O_2 adsorbed on the surface of $Ni_8/CrBr_3$. Further combined with the d-band center, $Ni_2/CrBr_3$ and $Ni_8/CrBr_3$ have similar d-band centers and are far from the Fermi level, so the two catalysts have the same selectivity for ORR. The adsorption energy of O_2 can also indirectly react the catalytic selectivity of the catalyst for ORR. Generally speaking, the stronger the adsorption energy of O_2, the more unfavorable the synthesis of H_2O_2. This is because the higher adsorption energy of O_2 causes electrons to flow from the *d* orbital of the transition metal into the antibonding orbital of O_2, which reduces the bonding order of O_2. The ORR selectivity of $Ni_1/CrBr_3$, $Ni_2/CrBr_3$ and $Ni_8/CrBr_3$ catalysts is $4e^-$ ORR, $2e^-$ ORR, $2e^-$ ORR, respectively, which is exactly in line with the judgment of adsorption energy on the selectivity of catalyst ORR.

It has been proved previously that the phase temperature Tc of $Ni_1/CrBr_3$, $Ni_2/CrBr_3$ and $Ni_8/CrBr_3$ catalysts is much lower than room temperature. Although FIM is the ground state among these three catalysts, given the room temperature electrocatalytic reaction, magnetic states below their respective phase transition temperatures are not relevant for catalytic activity assessment. The effect of different arrangement of AFM states on catalytic performance of different catalysts was compared, as shown in Figure 5(a-c). It was found that the catalytic performance of $2e^-$ ORR and $4e^-$ ORR was improved by changing the magnetic arrangement of the AFM

state of the catalyst. The overpotential of the $4e^-$ ORR reaction on $Ni_1/CrBr_3$ reaches 0.29 V in the AFM4, which is 0.08 V higher than that of the ground state FIM (0.37 V). For $Ni_2/CrBr_3$ and $Ni_8/CrBr_3$ catalysts, altering their AFM arrangement resulted in remarkable overpotential reduction for $2e^-$ ORR, reaching 0.01 V respectively. The overpotential disparity between different AFM states was significant. Specifically, the overpotential for AFM1 and AFM2 magnetic states of $Ni_2/CrBr_3$ and $Ni_8/CrBr_3$ on $2e^-$ ORR was 0.09 V and 0.25 V respectively, indicating precise regulation of catalyst ORR performance by adjusting magnetic state. In this vein, the pathway selective transformation of $4e^-$ ORR and $2e^-$ ORR is realized by regulating the presence of central vacancy Ni-Ni metal bond, and the activity of ORR reaction is promoted by regulating the overall magnetic arrangement of catalyst. Moreover, it is also necessary to consider side reaction of HER competition during the whole ORR. HER consumes protons and electrons directly in the electrocatalysis process, which reduces the Faraday efficiency of ORR. It is generally believed that the free energy of an ideal HER catalyst is close to zero ($\Delta G(*H) = 0$ eV). The adsorption energies (0.51 eV for $Ni_1/CrBr_3$, 0.66 eV for $Ni_2/CrBr_3$ and 0.72 eV for $Ni_8/CrBr_3$) of *H demonstrates H species do not adsorb on three catalysts, while O_2 features weak chemisorption or physisorption with the adsorption energies of -0.65 eV for $Ni_1/CrBr_3$, -0.31 eV for $Ni_2/CrBr_3$ and -0.46 eV for $Ni_8/CrBr_3$, respectively. Such differences indicate that the active sites on these three catalysts are more easily occupied by O_2. Obviously, HER performance is far inferior to ORR, which makes ORR more selective (99.9%) over $Ni_1/CrBr_3$, $Ni_2/CrBr_3$, and $Ni_8/CrBr_3$, as shown in the Figure 5d.

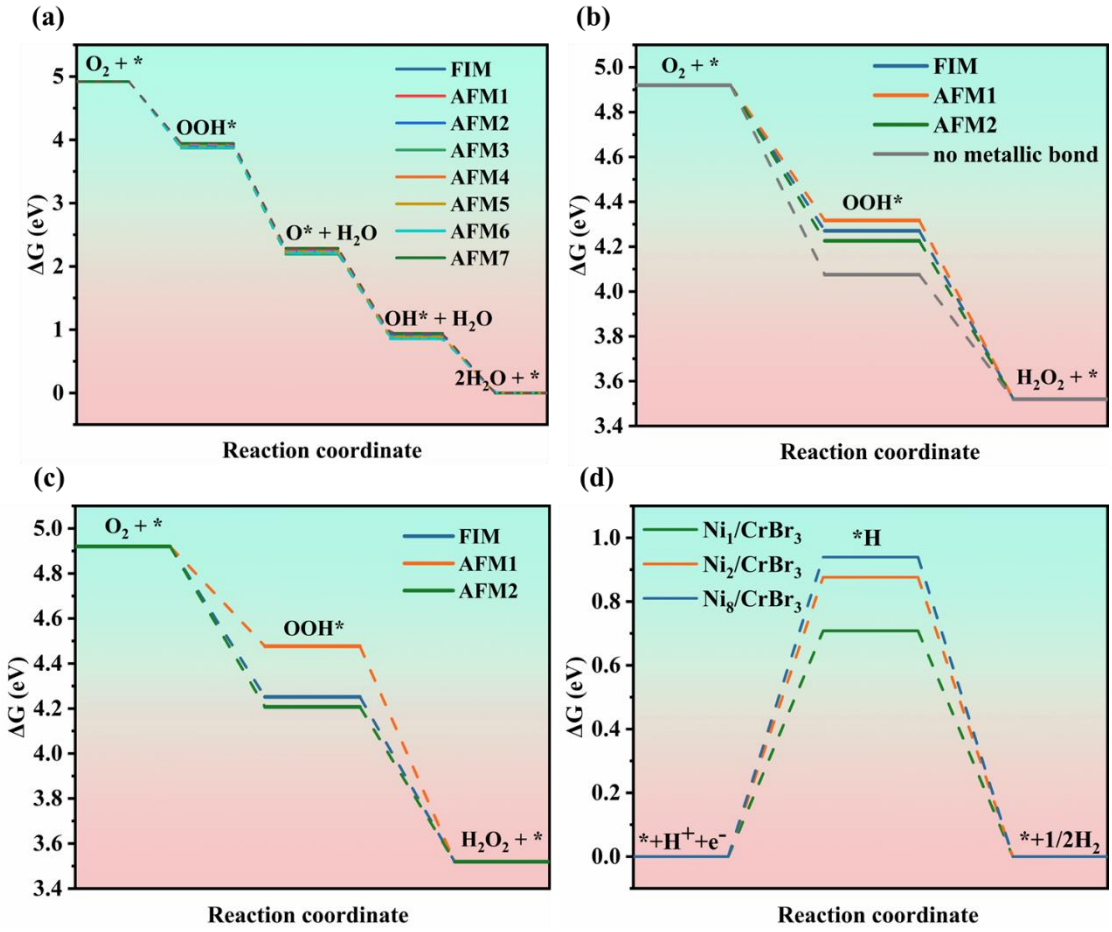

Fig. 5. The computed thermodynamic free energy for $Ni_1/CrBr_3$ 4e$^-$ ORR (a), $Ni_2/CrBr_3$ 2e$^-$ ORR (b), $Ni_8/CrBr_3$ 2e$^-$ ORR (c). The thermodynamic free energy of HER (d).

3.5 Effect of Applied Potential on Catalytic Properties of $Ni_x/CrBr_3$

Previous calculations utilized the widely employed CHE model in electrocatalysis simulations, known for its simplicity yet significant success in elucidating reaction mechanisms and predicting ORR catalysts.[64] However, the model falls short in accurately accounting for the effect of applied potentials on catalytic properties due to the fixed electron number with conventional canonical-ensemble algorithm, resulting in the inaccurate description in the effect of pH and electrode potential on free energy.[65, 66] To address this issue, electrocatalysis simulations under the applied potential were carried out using a uniform charge background to compensate the surface excess charges[67-70]. The most stable or highest ORR catalytic activity magnetic states of the three catalysts were taken into account as depicted in Figure S14.

In aforementioned CHE calculations, $Ni_1/CrBr_3$ was found to undergo a $4e^-$ ORR reaction, while $Ni_2/CrBr_3$ and $Ni_8/CrBr_3$ favor a $2e^-$ ORR reaction. Employing the CPM mechanism, the most stable magnetic states or those with the best catalytic performance were selected for the three catalysts. All ORR pathway intermediates were optimized under various charges, and their energies were depicted as functions of the applied electrode potential relative to the SHE, as illustrated in Figure S15-17. Energy dependence on potential was effectively represented by a parabolic function, with fitting parameters detailed in Tables S4-6. By analyzing the energy derived from the potential dependence of reaction intermediates, pH-dependent free energy distribution and corresponding onset potentials were determined. The energies of intermediate corresponding to different magnetic states of different catalysts were analyzed in terms of both individual catalytic pathways and the overall catalytic pathway. The quadratic parabolic curves depicting the variation of intermediate energies with applied potentials (relative to the SHE) for different magnetic states of the catalysts were integrated. For clarity, Figure 6 only displays the *OOH and *OH fitted polynomial curves, while pure catalyst and *O detailed fitting information can be found in Figure S18-19. It can be observed that the energies of the intermediates associated with different magnetic states undergo varying degrees of change with the applied potential during the catalytic process. Consequently, adjusting the applied potential can cause energies of intermediates from various magnetic states to intersect, potentially leading to transitions between states. This suggests the ability to achieve desired changes in ORR catalytic activity or pathway selectivity by precisely controlling the applied potential during the reaction.

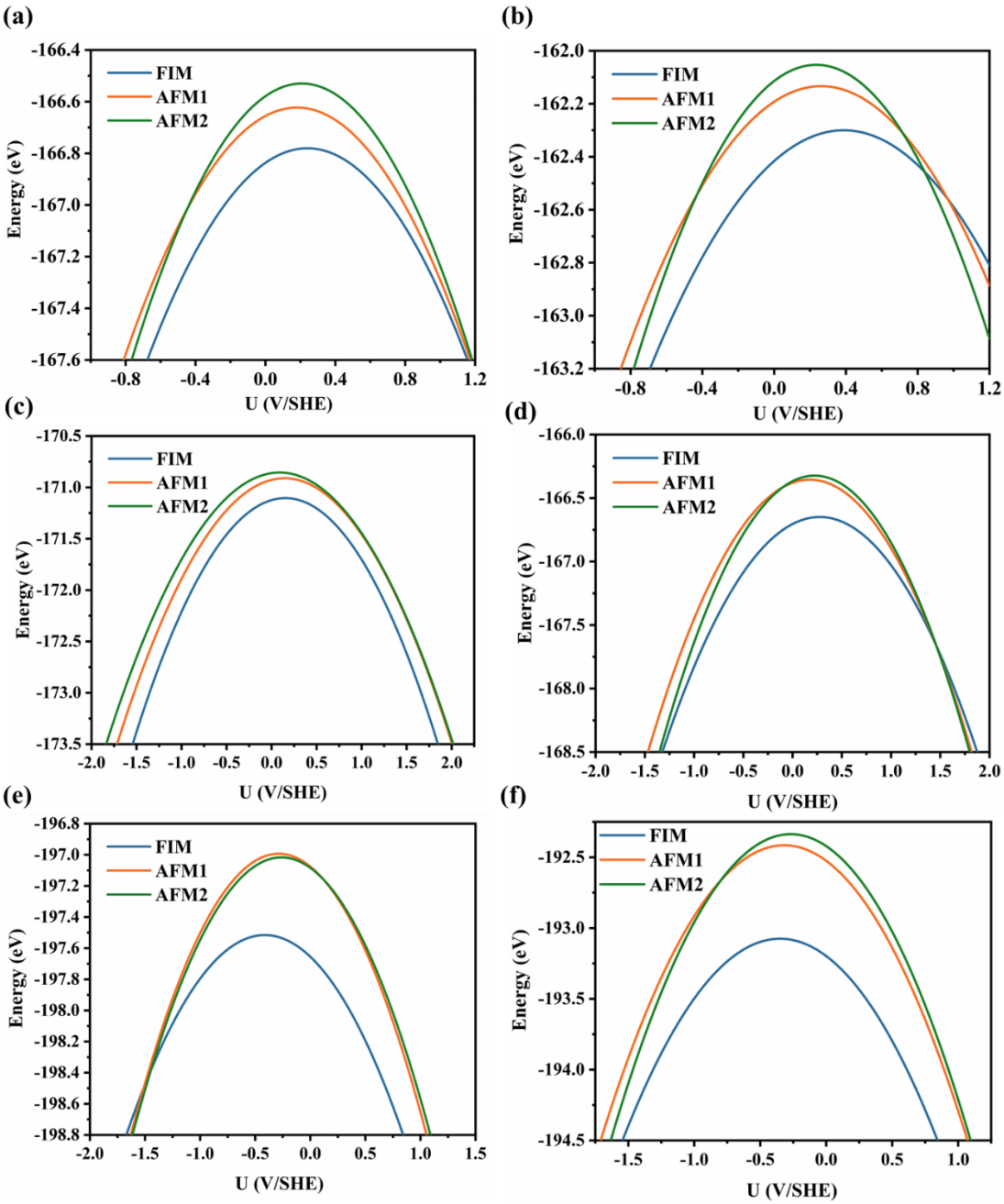

Fig. 6. Polynomial fits of various magnetic state of (a) *OOH-$Ni_1/CrBr_3$, (b) *OH-$Ni_1/CrBr_3$, (c) *OOH-$Ni_2/CrBr_3$, (d) *OH-$Ni_2/CrBr_3$, (e) *OOH-$Ni_8/CrBr_3$, (f) *OH-$Ni_8/CrBr_3$, as a function of potential. The calculated total energy values can be found in the Supporting Information.

For $Ni_1/CrBr_3$, the energies of *OOH and *OH intermediates exhibit an intersecting behavior with the applied potential (see Figure 6a-b). Typically, *OOH and *OH are crucial steps for the $2e^-$ ORR and $4e^-$ ORR rate-determining pathways, respectively, consistent with the previous analysis based on the CHE model for the three

catalysts. The energy intersection between *OOH and *OH is attributed to their different PZC. Due to the first-order Stark effect,[69] one state can be more stable than the other by biasing the potential (see Figure S20). The optimized $Ni_1/CrBr_3$ and the corresponding intermediates (*OOH, *O, and *OH) at zero charge can be found in the Figure S21. The adsorption energies of the three intermediates relative to the applied potentials are shown in Figure S24. The applied potential has the greatest influence on the adsorption energies of *OOH and *O, followed by *OH. These varying degrees of correlation will affect the RDS and onset potentials at different applied potentials and pH values. The pH-dependent free energy profiles and corresponding onset potentials (defined as the potentials at which the maximum free energy change is equal to 0) were obtained by combining the adsorption energies of the reaction intermediates with the reaction mechanism. As shown in the Figure 7(a-c), the onset potentials of the three magnetic states of $Ni_1/CrBr_3$ for ORR at pH = 1 were determined to be 0.79 V/RHE for FIM, 0.86 V/RHE for AFM1, and 0.83 V/RHE for AFM2, respectively. These values are higher than the values at pH = 13 (0.53 V/RHE for FIM, 0.64 V/RHE for AFM1, and 0.68 V/RHE for AFM2). This indicates that the ORR catalyzed by $Ni_1/CrBr_3$ is favorable in an acidic environment. The RDS for all magnetic states is the removal of *OH, consistent with the previous CHE calculations, suggesting the strong adsorption of *OH on $Ni_1/CrBr_3$. The Figure 7(d-f) shows the pH and potential-dependent contour plots of the adsorption energy of *OH on $Ni_1/CrBr_3$ in the three magnetic states. It can be observed that the adsorption strength of *OH on $Ni_1/CrBr_3$ increases with increasing pH or decreasing applied potential. Hence, in an alkaline environment, the removal of *OH becomes more challenging, offering an explanation for the pH-dependent activity of $Ni_1/CrBr_3$.

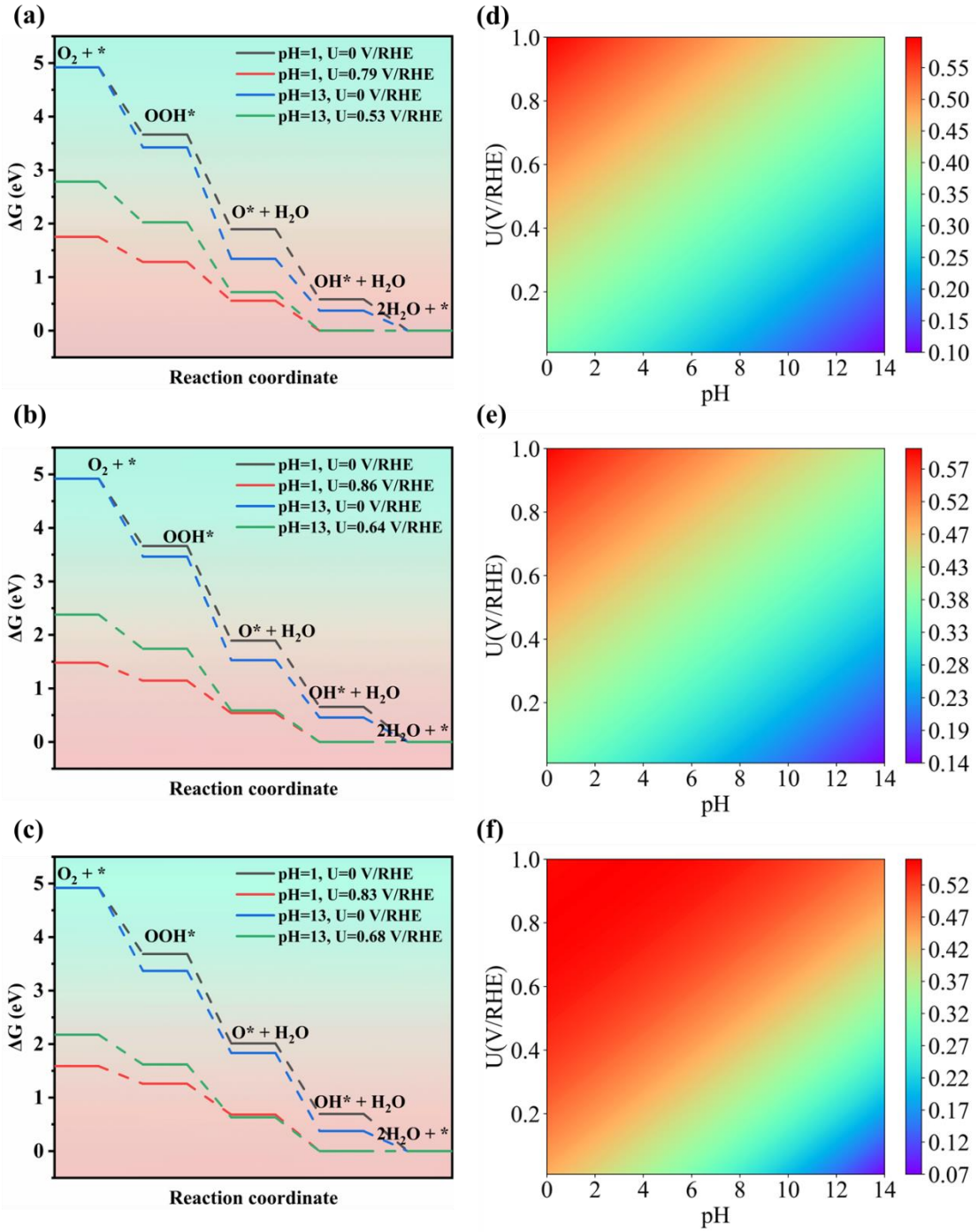

Fig. 7. Free energy diagrams of the ORR on (a) FIM $Ni_1/CrBr_3$, (b) AFM1 $Ni_1/CrBr_3$, (c) AFM2 $Ni_1/CrBr_3$. pH-dependent and potential-dependent contour plot of adsorption energies of *OH on (d) FIM $Ni_1/CrBr_3$, (e) AFM1 $Ni_1/CrBr_3$, (f) AFM2 $Ni_1/CrBr_3$.

It has been previously demonstrated that the catalyst's transformation to $Ni_2/CrBr_3$ leads to a transition in the selectivity of the ORR catalytic pathway from $4e^-$ ORR to $2e^-$ ORR. The optimized structures of $Ni_2/CrBr_3$ and the corresponding intermediates (*OOH, *O, and *OH) without doped charge are shown in Figure S22, and the

adsorption energies of the three intermediates relative to the applied potential are shown in Figure S25. The applied potential has the greatest impact on *O adsorption energy, followed by *OOH, while its effect on *OH is relatively minor. According to Figure 6c-d, the ORR intermediates *OOH and *OH in $Ni_2/CrBr_3$ exhibit spin crossover phenomena as well. The pH-dependent free energy profiles and the corresponding onset potentials (at which the maximum free energy change is zero) based on the RHE scale were obtained. As shown in the Figure 8(a-c), the onset potentials of the three magnetic states for ORR at pH = 1 were determined to be 0.87 V/RHE for FIM, 0.92 V/RHE for AFM1, and 0.93 V/RHE for AFM2, respectively, slightly lower than the values at pH = 13 (0.88 V/RHE for FIM, 0.99 V/RHE for AFM1, and 0.95 V/RHE for AFM2). The free energy pathway diagram suggests that for $Ni_2/CrBr_3$ under CPM, the RDS of the ORR catalytic pathway is the *OOH formation step, consistent with the result calculated by CHE. Figure 8(d-f) illustrates pH and potential-dependent contour plots of *OOH adsorption energy on the three magnetic states of $Ni_2/CrBr_3$. For FIM and AFM1, *OOH adsorption strength increases with rising pH or decreasing potential, while for AFM2, it initially rises and then declines under similar conditions. At determined onset potential and pH levels, *OOH adsorption energy remains relatively constant for FIM and AFM2 between pH = 1 and pH = 13, yielding similar calculated onset potentials across different pH conditions. At pH = 13, AFM1 exhibits a notable rise in *OOH adsorption energy compared to pH = 1, promoting its adsorption onto the $Ni_2/CrBr_3$ surface in alkaline conditions. This phenomenon facilitates *OOH formation, elucidating the pH-dependent activity of $Ni_2/CrBr_3$.

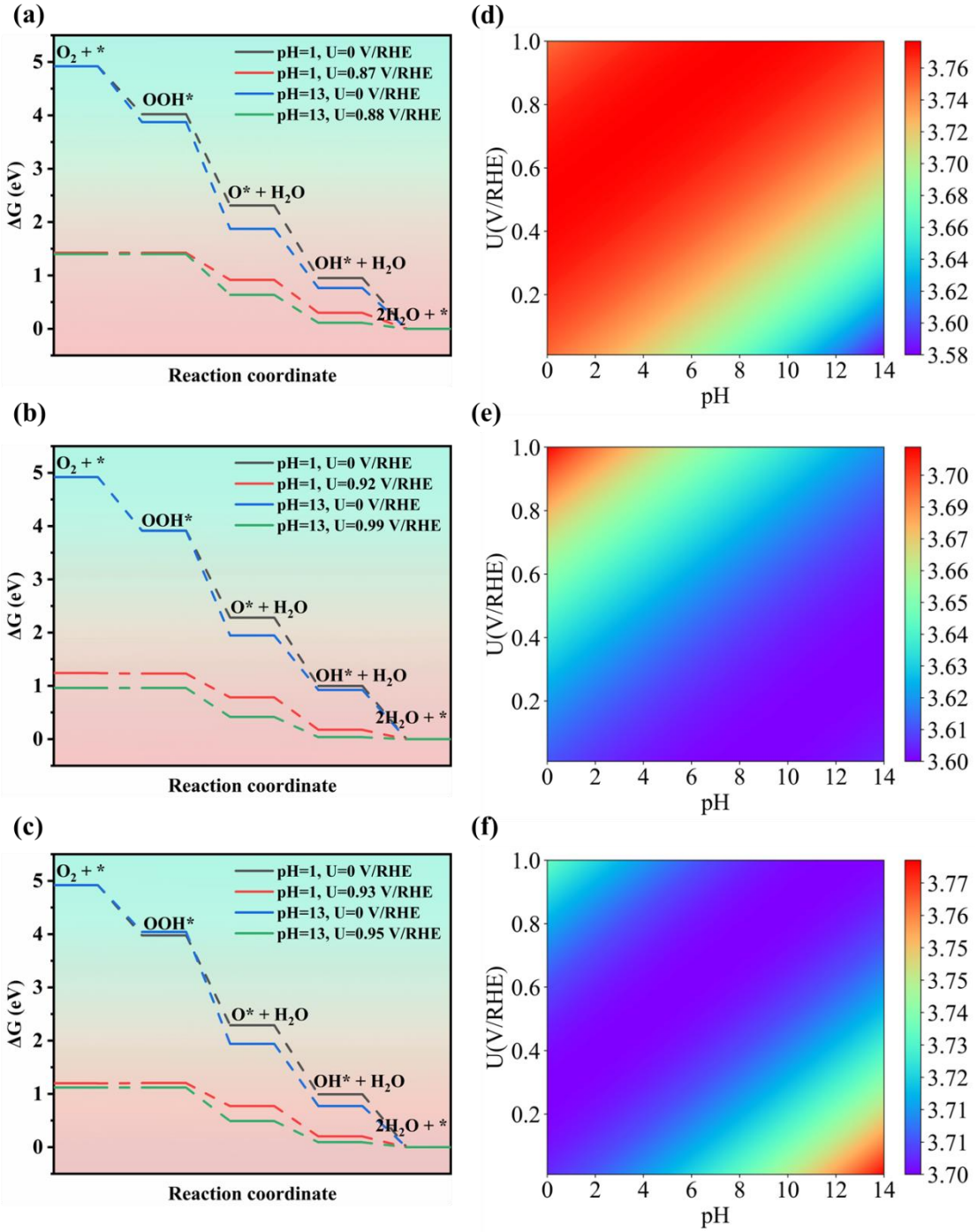

Fig. 8. Free energy diagrams of the ORR on (a) FIM $Ni_2/CrBr_3$, (b) AFM1 $Ni_2/CrBr_3$, (c) AFM2 $Ni_2/CrBr_3$. pH-dependent and potential-dependent contour plot of adsorption energies of *OOH on (d) FIM $Ni_2/CrBr_3$, (e) AFM1 $Ni_2/CrBr_3$, (f) AFM2 $Ni_2/CrBr_3$.

For $Ni_8/CrBr_3$, the intermediates (*OOH, *O, and *OH) were optimized at zero charge as depicted in Figure S23, and the adsorption energies relative to the applied potentials are shown in Figure S26. These intermediates show a distinct dependency on applied potential compared to previous catalyst types. The influence of applied

potential on adsorption energies varies across intermediates and magnetic states. Notably, *OH adsorption energy is most affected in FIM and AFM2, while *OOH and *O exhibit similar changes. Conversely, in AFM1, *O is most affected, followed by *OH and *OOH. The dependence of adsorption energies on the applied potential shows distinct differences from the previous discussion. Additionally, the spin crossover in *OOH and *OH intermediates is once again observed in the ORR process (see Figure 6e-f). This difference may be related to the variation in the RDS of the reaction pathway. Furthermore, significant changes in the configurations between *OH and *OOH (see Figure S30-32) can be observed among the different magnetic states. With changes in the magnetic state and applied potential, the distance of Ni atoms protruding from the plane and the ∠NiOO of *OOH in AFM1 are smaller than those in AFM2, while the Ni-O bond length remains relatively unchanged. Regarding *OH, with changes in the magnetic state and applied potential, the distance of Ni protruding from the plane in AFM2 is generally smaller than that in AFM1, and ∠NiOH is smaller in AFM2 than in AFM1 before an applied potential of 0.1 V/SHE. However, after an applied potential greater than 0.1 V/SHE, ∠NiOH in AFM2 surpasses that in AFM1. Catalytically, the ORR onset potentials for the three magnetic states shown in the Figure 9(a-c), at pH = 1 are determined to be 0.81 V/RHE for FIM, 0.89 V/RHE for AFM1, and 0.87 V/RHE for AFM2, respectively, which are lower than those at pH = 13, which are 0.86 V/RHE for FIM, 0.93 V/RHE for AFM1, and 0.90 V/RHE for AFM2. In reaction pathways, FIM and AFM2 favor $2e^-$ ORR with *OOH formation as the RDS, while under AFM1 magnetic state, the ORR pathway shifts to $4e^-$ ORR under acidic conditions, with the RDS transitioning to *OH removal. Figure 9(d-f) illustrates contour plots showing the pH and potential dependency of *OOH and *OH adsorption energies on $Ni_8/CrBr_3$ magnetic states. Higher pH or lower applied potential enhances *OOH adsorption strength on FIM and AFM2 of $Ni_8/CrBr_3$. Hence, the alkaline environment promotes *OOH adsorption on $Ni_8/CrBr_3$, elucidating the elevated initial potential observed in alkaline conditions. Interestingly, as the pH increases, the RDS for AFM1 shifts from the removal of *OH to the formation of *OOH. In Figure S29, we plotted the difference

between the adsorption energies of *OH and *OOH, and this difference increases slightly with changes in the applied potential. According to the eq 5, when *U*/RHE is fixed, different pH values lead to different *U*/SHE. This variation can account for the change in the RDS and consequently the shift in the selectivity of the ORR pathway on the $Ni_8/CrBr_3$ catalyst from $4e^-$ ORR to $2e^-$ ORR.

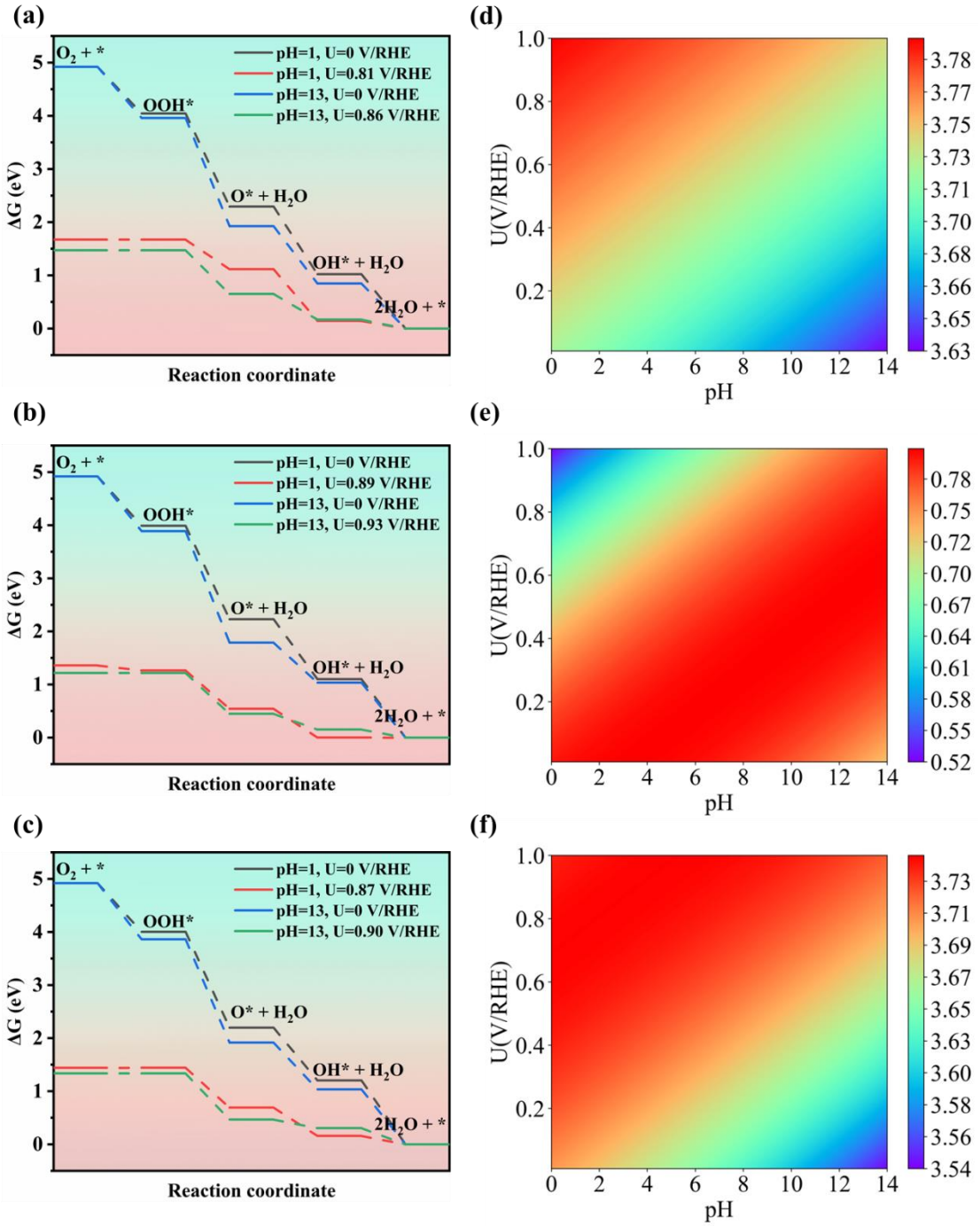

Fig. 9. Free energy diagrams of the ORR on (a) FIM $Ni_8/CrBr_3$, (b) AFM1 $Ni_8/CrBr_3$, (c) AFM2 $Ni_8/CrBr_3$. pH-dependent and potential-dependent contour plot of adsorption

energies of *OOH on (d) FIM $Ni_8/CrBr_3$, *OH on (e) AFM1 $Ni_8/CrBr_3$, and *OOH on (f) AFM2 $Ni_8/CrBr_3$.

The preceding discussion primarily focused on the potential variation of the ORR reaction pathway resulting from pH and external potential changes within the same magnetic state of a similar catalyst, namely $Ni_1/CrBr_3$, $Ni_2/CrBr_3$, and $Ni_8/CrBr_3$. A selective transition was observed in the ORR pathway within AFM1 of $Ni_8/CrBr_3$. Subsequently, a comparison was made between different magnetic states of the identical catalyst under consistent pH conditions. It is worth noting that a pathway selectivity transition between AFM1 and AFM2 of $Ni_8/CrBr_3$ was also observed under pH = 1, as depicted in Figure 9(b-c). In AFM1, the main pathway is $4e^-$ ORR, while in AFM2, it mainly undergoes $2e^-$ ORR. Furthermore, it was observed that the onset potentials of the two pathways in AFM1 and AFM2 differ by merely 0.02 V/RHE. This implies that by simply changing the different antiferromagnetic states of $Ni_8/CrBr_3$ and applying a small external voltage, the control of the ORR pathway can be achieved, and high ORR catalytic activity can be obtained. Furthermore, by examining the energy and external potential variation of the same intermediate during ORR on different magnetic states of $Ni_8/CrBr_3$ at the corresponding onset potential, as shown in Figure 6(e-f). The energy levels of AFM1 and AFM2 were found to be in close proximity, indicating the potential for regulating the pathway transition between magnetic states.

Conclusions

In conclusion, we thoroughly examined the impact of ferromagnetic support on ORR properties across three different loading Ni-loaded $Ni_x/CrBr_3$ catalysts with different magnetic configurations. The resultant $Ni_x/CrBr_3$ feature FIM properties with because of antiferromagnetic exchange of Ni-Cr, and the introduction of Ni-Ni metal bonds induces direct ferromagnetic interaction, resulting in magnetic phase temperature increases. Introduction of Ni-Ni metal bonds directly connected to the active sites enabled a weakening of O_2 adsorption. With the increase of Ni loading, the easy magnetic axis transitions from out-of-plane (2D-Heisenberg) to in-plane (2D-XY). Additionally, the adsorption properties of $Ni_x/CrBr_3$, including O_2 adsorption energy

and configuration, are independent of the *d*-band center and closely tied to magnetic anisotropy. More notably, both applied potential and electrolyte acidity are crucial factors triggering magnetic transition phenomena during the ORR, causing a shift in the catalytic pathway from $4e^-$ ORR to $2e^-$ ORR. This results in achieving an excellent onset potential of 0.93 V/RHE. Generally, these findings present novel strategy for understanding and designing heterogeneous electrocatalysts.

Supporting Information

The Supporting Information contains detailed information: geometrical structures, DOS analysis, electronic structure, calculated energies as a function of the applied potential and free energy profile, the changes of Gibbs free energy, pH-dependent and potential-dependent contour plot of adsorption energies and difference of adsorption energies and so on.

Author Information

Corresponding Author

*Email: glzhuang@zjut.edu.cn (G. L. Zhuang)

Author Contributions

Yi-jie Chen: Methodology, Validation, Investigation, Data curation, Writing-Original Draft, Writing-Review & Editing; **Jun Wen:** Data curation, Writing-Original Draft, Writing-Review & Editing; **Zhi-rui Luo, Wen-xian Chen**: Data curation, Writing-Review & Editing; **Gui-lin Zhuang:** Conceptualization, Software, Resources, Writing-Review & Editing, Supervision.

Acknowledgement

This work was supported by the National Natural Science Foundation of China (Grant No: 22072135, 22022108), Zhejiang Provincial Natural Science Foundation of China (Grant No: LTGY23B010001), Natural Science Foundation of Shandong

Province (ZR2020ZD35).

Conflicts of interest

The authors declare no competing financial interest.

Reference

(1) Hage, R.; Lienke, A. Applications of Transition-Metal Catalysts to Textile and Wood-Pulp Bleaching. *Angew. Chem. Int. Ed.* **2006**, *45*, 206-222.
(2) Enache, D. I.; Edwards, J. K.; Landon, P.; Solsona-Espriu, B.; Carley, A. F.; Herzing, A. A.; Watanabe, M.; Kiely, C. J.; Knight, D. W.; Hutchings, G. J. Solvent-Free Oxidation of Primary Alcohols to Aldehydes Using Au-Pd/TiO2 Catalysts. *Science* **2006**, *311*, 362-365.
(3) Qi, J.; Du, Y.; Yang, Q.; Jiang, N.; Li, J.; Ma, Y.; Ma, Y.; Zhao, X.; Qiu, J. Energy-saving and product-oriented hydrogen peroxide electrosynthesis enabled by electrochemistry pairing and product engineering. *Nat. Commun.* **2023**, *14*, 6263.
(4) Wang, Z.; Gao, B.; Liu, J.; Sillanpää, M.; Kim, Y. The oxidation treatment of pharmaceutical wastewater in H2O2 and PMS system by Iron-containing biochar originated from excess sludge. *J. Water Process Eng.* **2024**, *58*, 104833.
(5) Martínez-Huitle, C. A.; Panizza, M. Electrochemical oxidation of organic pollutants for wastewater treatment. *Curr. Opin. Electrochem.* **2018**, *11*, 62-71.
(6) Hou, H.; Zeng, X.; Zhang, X. Production of Hydrogen Peroxide by Photocatalytic Processes. *Angew. Chem. Int. Ed.* **2020**, *59*, 17356-17376.
(7) Krivtsov, I.; Mitoraj, D.; Adler, C.; Ilkaeva, M.; Sardo, M.; Mafra, L.; Neumann, C.; Turchanin, A.; Li, C.; Dietzek, B.; et al. Water-Soluble Polymeric Carbon Nitride Colloidal Nanoparticles for Highly Selective Quasi-Homogeneous Photocatalysis. *Angew. Chem. Int. Ed.* **2020**, *59*, 487-495.
(8) Campos-Martin, J. M.; Blanco-Brieva, G.; Fierro, J. L. G. Hydrogen Peroxide Synthesis: An Outlook beyond the Anthraquinone Process. *Angew. Chem. Int. Ed.* **2006**, *45*, 6962-6984.
(9) Zhang, W.; Sun, F.-L.; Fang, Q.-J.; Yu, Y.-F.; Pan, J.-K.; Wang, J.-G.; Zhuang, G.-L. Synergistic Effect of Coordination Fields and Hydrosolvents on the Single-Atom Catalytic Property in H2O2 Synthesis: A Density Functional Theory Study. *J. Phys. Chem. C* **2022**, *126*, 2349-2364.
(10) Wu, Q.; Cao, J.; Wang, X.; Liu, Y.; Zhao, Y.; Wang, H.; Liu, Y.; Huang, H.; Liao, F.; Shao, M.; et al. A metal-free photocatalyst for highly efficient hydrogen peroxide photoproduction in real seawater. *Nat. Commun.* **2021**, *12*, 483.
(11) Zhang, Y.; Lyu, Z.; Chen, Z.; Zhu, S.; Shi, Y.; Chen, R.; Xie, M.; Yao, Y.; Chi, M.; Shao, M.; et al. Maximizing the Catalytic Performance of Pd@AuxPd1−x Nanocubes in H2O2 Production by Reducing Shell Thickness to Increase Compositional Stability. *Angew. Chem. Int. Ed.* **2021**, *60*, 19643-19647.
(12) Flaherty, D. W. Direct Synthesis of H2O2 from H2 and O2 on Pd Catalysts: Current

729 Understanding, Outstanding Questions, and Research Needs. *ACS Catal.* **2018**, *8*, 1520-
730 1527.
731 (13) Hu, B.; Deng, W.; Li, R.; Zhang, Q.; Wang, Y.; Delplanque-Janssens, F.; Paul, D.;
732 Desmedt, F.; Miquel, P. Carbon-supported palladium catalysts for the direct synthesis
733 of hydrogen peroxide from hydrogen and oxygen. *J. Catal.* **2014**, *319*, 15-26.
734 (14) Arrigo, R.; Schuster, M. E.; Abate, S.; Giorgianni, G.; Centi, G.; Perathoner, S.;
735 Wrabetz, S.; Pfeifer, V.; Antonietti, M.; Schlögl, R. Pd Supported on Carbon Nitride
736 Boosts the Direct Hydrogen Peroxide Synthesis. *ACS Catal.* **2016**, *6*, 6959-6966.
737 (15) Gervasini, A.; Carniti, P.; Desmedt, F.; Miquel, P. Liquid Phase Direct Synthesis
738 of H2O2: Activity and Selectivity of Pd-Dispersed Phase on Acidic Niobia-Silica
739 Supports. *ACS Catal.* **2017**, *7*, 4741-4752.
740 (16) Zhang, C.; Lu, R.; Liu, C.; Yuan, L.; Wang, J.; Zhao, Y.; Yu, C. High Yield
741 Electrosynthesis of Hydrogen Peroxide from Water Using Electrospun
742 CaSnO3@Carbon Fiber Membrane Catalysts with Abundant Oxygen Vacancy. *Adv.*
743 *Funct. Mater.* **2021**, *31*, 2100099.
744 (17) Kim, K.-H.; Kim, S.-J.; Choi, W. H.; Lee, H.; Moon, B. C.; Kim, G. H.; Choi, J.
745 W.; Park, D. G.; Choi, J. H.; Kim, H.; et al. Triphasic Metal Oxide Photocatalyst for
746 Reaction Site-Specific Production of Hydrogen Peroxide from Oxygen Reduction and
747 Water Oxidation. *Adv. Energy Mater.* **2022**, *12*, 2104052.
748 (18) Sun, G.; Li, M. M.-J.; Nakagawa, K.; Li, G.; Wu, T.-S.; Peng, Y.-K. Bulk-to-nano
749 regulation of layered metal oxide gears H2O2 activation pathway for its stoichiometric
750 utilization in selective oxidation reaction. *Appl. Catal., B* **2022**, *313*, 121461.
751 (19) Bukas, V. J.; Kim, H. W.; Sengpiel, R.; Knudsen, K.; Voss, J.; McCloskey, B. D.;
752 Luntz, A. C. Combining Experiment and Theory To Unravel the Mechanism of Two-
753 Electron Oxygen Reduction at a Selective and Active Co-catalyst. *ACS Catal.* **2018**, *8*,
754 11940-11951.
755 (20) Kim, H. W.; Ross, M. B.; Kornienko, N.; Zhang, L.; Guo, J.; Yang, P.; McCloskey,
756 B. D. Efficient hydrogen peroxide generation using reduced graphene oxide-based
757 oxygen reduction electrocatalysts. *Nat. Catal.* **2018**, *1*, 282-290.
758 (21) Yan, Q.-Q.; Wu, D.-X.; Chu, S.-Q.; Chen, Z.-Q.; Lin, Y.; Chen, M.-X.; Zhang, J.;
759 Wu, X.-J.; Liang, H.-W. Reversing the charge transfer between platinum and sulfur-
760 doped carbon support for electrocatalytic hydrogen evolution. *Nat. Commun.* **2019**, *10*,
761 4977.
762 (22) Shi, Y.; Ma, Z.-R.; Xiao, Y.-Y.; Yin, Y.-C.; Huang, W.-M.; Huang, Z.-C.; Zheng,
763 Y.-Z.; Mu, F.-Y.; Huang, R.; Shi, G.-Y.; et al. Electronic metal–support interaction
764 modulates single-atom platinum catalysis for hydrogen evolution reaction. *Nat.*
765 *Commun.* **2021**, *12*, 3021.
766 (23) Parastaev, A.; Muravev, V.; Huertas Osta, E.; van Hoof, A. J. F.; Kimpel, T. F.;
767 Kosinov, N.; Hensen, E. J. M. Boosting CO2 hydrogenation via size-dependent metal–
768 support interactions in cobalt/ceria-based catalysts. *Nat. Catal.* **2020**, *3*, 526-533.
769 (24) van Deelen, T. W.; Hernández Mejía, C.; de Jong, K. P. Control of metal-support
770 interactions in heterogeneous catalysts to enhance activity and selectivity. *Nat. Catal.*
771 **2019**, *2*, 955-970.
772 (25) Ren, C.; Lu, S.; Wu, Y.; Ouyang, Y.; Zhang, Y.; Li, Q.; Ling, C.; Wang, J. A

Universal Descriptor for Complicated Interfacial Effects on Electrochemical Reduction Reactions. *J. Am. Chem. Soc.* **2022**, *144*, 12874-12883.
(26) Xin, H.; Vojvodic, A.; Voss, J.; Nørskov, J. K.; Abild-Pedersen, F. Effects of d-band shape on the surface reactivity of transition-metal alloys. *Phys. Rev. B* **2014**, *89*, 115114.
(27) Cao, A.; Nørskov, J. K. Spin Effects in Chemisorption and Catalysis. *ACS Catal.* **2023**, *13*, 3456-3462.
(28) Bhattacharjee, S.; Waghmare, U. V.; Lee, S.-C. An improved d-band model of the catalytic activity of magnetic transition metal surfaces. *Sci. Rep.* **2016**, *6*, 35916.
(29) Kresse, G.; Furthmüller, J. Efficient iterative schemes for ab initio total-energy calculations using a plane-wave basis set. *Phys. Rev. B* **1996**, *54*, 11169-11186.
(30) Ernzerhof, M.; Perdew, J. P. Generalized gradient approximation to the angle- and system-averaged exchange hole. *J. Chem. Phys.* **1998**, *109*, 3313-3320.
(31) Perdew, J. P.; Burke, K.; Ernzerhof, M. Generalized Gradient Approximation Made Simple. *Phys. Rev. Lett.* **1996**, *77*, 3865-3868.
(32) Blöchl, P. E. Projector augmented-wave method. *Phys. Rev. B* **1994**, *50*, 17953-17979.
(33) Dudarev, S. L.; Botton, G. A.; Savrasov, S. Y.; Humphreys, C. J.; Sutton, A. P. Electron-energy-loss spectra and the structural stability of nickel oxide: An LSDA+U study. *Phys. Rev. B* **1998**, *57*, 1505-1509.
(34) German, E.; Faccio, R.; Mombrú, A. W. A DFT + U study on structural, electronic, vibrational and thermodynamic properties of TiO2 polymorphs and hydrogen titanate: tuning the Hubbard 'U-term'. *J. Phys. Commun.* **2017**, *1*, 055006.
(35) Baldereschi, A. Mean-Value Point in the Brillouin Zone. *Phys. Rev. B* **1973**, *7*, 5212-5215.
(36) Grimme, S.; Antony, J.; Ehrlich, S.; Krieg, H. A consistent and accurate ab initio parametrization of density functional dispersion correction (DFT-D) for the 94 elements H-Pu. *J. Chem. Phys.* **2010**, *132*, 154104.
(37) Momma, K.; Izumi, F. VESTA 3 for three-dimensional visualization of crystal, volumetric and morphology data. *J. Appl. Crystallogr.* **2011**, *44*, 1272-1276.
(38) Wang, V.; Xu, N.; Liu, J.-C.; Tang, G.; Geng, W.-T. VASPKIT: A user-friendly interface facilitating high-throughput computing and analysis using VASP code. *Comput. Phys. Commun.* **2021**, *267*, 108033.
(39) Guo, X.; Gu, J.; Lin, S.; Zhang, S.; Chen, Z.; Huang, S. Tackling the Activity and Selectivity Challenges of Electrocatalysts toward the Nitrogen Reduction Reaction via Atomically Dispersed Biatom Catalysts. *J. Am. Chem. Soc.* **2020**, *142*, 5709-5721.
(40) Hu, X.; Chen, S.; Chen, L.; Tian, Y.; Yao, S.; Lu, Z.; Zhang, X.; Zhou, Z. What is the Real Origin of the Activity of Fe–N–C Electrocatalysts in the O2 Reduction Reaction? Critical Roles of Coordinating Pyrrolic N and Axially Adsorbing Species. *J. Am. Chem. Soc.* **2022**, *144*, 18144-18152.
(41) Fishman, M. P.; Zhuang, H. L.; Mathew, K.; Dirschka, W.; Hennig, R. G. Accuracy of exchange-correlation functionals and effect of solvation on the surface energy of copper. *Phys. Rev. B* **2013**, *87*, 245402.
(42) Mathew, K.; Sundararaman, R.; Letchworth-Weaver, K.; Arias, T. A.; Hennig, R.

G. Implicit solvation model for density-functional study of nanocrystal surfaces and reaction pathways. *J. Chem. Phys.* **2014**, *140*, 084106.
(43) Liu, L.; Chen, S.; Lin, Z.; Zhang, X. A Symmetry-Breaking Phase in Two-Dimensional FeTe2 with Ferromagnetism above Room Temperature. *J. Phys. Chem. Lett.* **2020**, *11*, 7893-7900.
(44) Zhang, Z.; Shang, J.; Jiang, C.; Rasmita, A.; Gao, W.; Yu, T. Direct Photoluminescence Probing of Ferromagnetism in Monolayer Two-Dimensional CrBr3. *Nano Lett.* **2019**, *19*, 3138-3142.
(45) Webster, L. G.; Yan, J.-A. Strain-tunable magnetic anisotropy in monolayer CrCl3 , CrBr3 , and CrI3. *Phys. Rev. B* **2018**, *98*, 144411.
(46) Zhang, W.-B.; Qu, Q.; Zhu, P.; Lam, C.-H. Robust Intrinsic Ferromagnetism and Half Semiconductivity in Stable Two-Dimensional Single-Layer Chromium Trihalides. *J. Mater. Chem. C* **2015**, *3*, 12457-12468.
(47) Kvashnin, Y. O.; Bergman, A.; Lichtenstein, A. I.; Katsnelson, M. I. Relativistic exchange interactions in CrX3 (X=Cl , Br, I) monolayers. *Phys. Rev. B* **2020**, *102*, 115162.
(48) Tomar, S.; Ghosh, B.; Mardanya, S.; Rastogi, P.; Bhadoria, B. S.; Chauhan, Y. S.; Agarwal, A.; Bhowmick, S. Intrinsic magnetism in monolayer transition metal trihalides: A comparative study. *J. Magn. Magn. Mater.* **2019**, *489*, 165384.
(49) Medford, A. J.; Vojvodic, A.; Hummelshøj, J. S.; Voss, J.; Abild-Pedersen, F.; Studt, F.; Bligaard, T.; Nilsson, A.; Nørskov, J. K. From the Sabatier principle to a predictive theory of transition-metal heterogeneous catalysis. *J. Catal.* **2015**, *328*, 36-42.
(50) Hu, S.; Li, W.-X. Sabatier principle of metal-support interaction for design of ultrastable metal nanocatalysts. *Science* **2021**, *374*, 1360-1365.
(51) Henkelman, G.; Uberuaga, B. P.; Jónsson, H. A climbing image nudged elastic band method for finding saddle points and minimum energy paths. *J. Chem. Phys.* **2000**, *113*, 9901-9904.
(52) Henkelman, G.; Jónsson, H. Improved tangent estimate in the nudged elastic band method for finding minimum energy paths and saddle points. *J. Chem. Phys.* **2000**, *113*, 9978-9985.
(53) Wang, Y.; Xu, X.; Ji, W.; Li, S.; Li, Y.; Zhao, X. Exploitable magnetic anisotropy and half-metallicity controls in multiferroic van der Waals heterostructure. *npj Comput. Mater.* **2023**, *9*, 223.
(54) Logemann, R.; Rudenko, A. N.; Katsnelson, M. I.; Kirilyuk, A. Exchange interactions in transition metal oxides: the role of oxygen spin polarization. *J. Phys.: Condens. Matter* **2017**, *29*, 335801.
(55) Xiang, H.; Lee, C.; Koo, H.-J.; Gong, X.-G.; Whangbo, M.-H. Magnetic properties and energy-mapping analysis. *Dalton Trans.* **2013**, *42 4*, 823-853.
(56) Xiang, H. J.; Kan, E. J.; Wei, S.-H.; Whangbo, M. H.; Gong, X. G. Predicting the spin-lattice order of frustrated systems from first principles. *Phys. Rev. B* **2011**, *84*, 224429.
(57) Anderson, P. W. Antiferromagnetism. Theory of Superexchange Interaction. *Phys. Rev.* **1950**, *79*, 350-356.
(58) Kanamori, J. Superexchange interaction and symmetry properties of electron

orbitals. *J. Phys. Chem. Solids* **1959**, *10*, 87-98.
(59) Goodenough, J. B. An interpretation of the magnetic properties of the perovskite-type mixed crystals La1−xSrxCoO3−λ. *J. Phys. Chem. Solids* **1958**, *6*, 287-297.
(60) Frey, N. C.; Kumar, H.; Anasori, B.; Gogotsi, Y.; Shenoy, V. B. Tuning Noncollinear Spin Structure and Anisotropy in Ferromagnetic Nitride MXenes. *ACS Nano* **2018**, *12*, 6319-6325.
(61) Liu, W.; Tong, J.; Deng, L.; Yang, B.; Xie, G.; Qin, G.; Tian, F.; Zhang, X. Two-dimensional ferromagnetic semiconductors of rare-earth monolayer GdX2 (X = Cl, Br, I) with large perpendicular magnetic anisotropy and high Curie temperature. *Mater. Today Phys.* **2021**, *21*, 100514.
(62) Xie, L.; Wang, P.; Li, Y.; Zhang, D.; Shang, D.; Zheng, W.; Xia, Y.; Zhan, S.; Hu, W. Pauling-type adsorption of O2 induced electrocatalytic singlet oxygen production on N–CuO for organic pollutants degradation. *Nat. Commun.* **2022**, *13*, 5560.
(63) Zhang, W.; Gao, Y.-j.; Fang, Q.-J.; Pan, J.-k.; Zhu, X.-C.; Deng, S.-w.; Yao, Z.-h.; Zhuang, G.-l.; Wang, J.-g. High-performance single-atom Ni catalyst loaded graphyne for H2O2 green synthesis in aqueous media. *J. Colloid Interface Sci.* **2021**, *599*, 58-67.
(64) Nørskov, J. K.; Rossmeisl, J.; Logadottir, A.; Lindqvist, L.; Kitchin, J. R.; Bligaard, T.; Jónsson, H. Origin of the Overpotential for Oxygen Reduction at a Fuel-Cell Cathode. *J. Phys. Chem. B* **2004**, *108*, 17886-17892.
(65) Li, A.; Kong, S.; Guo, C.; Ooka, H.; Adachi, K.; Hashizume, D.; Jiang, Q.; Han, H.; Xiao, J.; Nakamura, R. Enhancing the stability of cobalt spinel oxide towards sustainable oxygen evolution in acid. *Nat. Catal.* **2022**, *5*, 109-118.
(66) Qian, S.-J.; Cao, H.; Chen, J.-W.; Chen, J.-C.; Wang, Y.-G.; Li, J. Critical Role of Explicit Inclusion of Solvent and Electrode Potential in the Electrochemical Description of Nitrogen Reduction. *ACS Catal.* **2022**, *12*, 11530-11540.
(67) Zhang, X.; Zhou, Z. Perspective on Theoretical Models for CO2 Electrochemical Reduction. *J. Phys. Chem. C* **2022**, *126*, 3820-3829.
(68) Hu, X.; Yao, S.; Chen, L.; Zhang, X.; Jiao, M.; Lu, Z.; Zhou, Z. Understanding the role of axial O in CO2 electroreduction on NiN4 single-atom catalysts via simulations in realistic electrochemical environment. *J. Mater. Chem. A* **2021**, *9*, 23515-23521.
(69) Duan, Z.; Henkelman, G. Surface Charge and Electrostatic Spin Crossover Effects in CoN4 Electrocatalysts. *ACS Catal.* **2020**, *10*, 12148-12155.
(70) Duan, Z.; Henkelman, G. Theoretical Resolution of the Exceptional Oxygen Reduction Activity of Au(100) in Alkaline Media. *ACS Catal.* **2019**, *9*, 5567-5573.